Nonlinear dynamics of surfactant–laden two–fluid Couette flows in the presence of inertia

A. K A L O G I R O U[1,2] † A N D D. T. P A P A G E O R G I O U[1]

[1]Department of Mathematics, Imperial College London, South Kensington Campus, London SW7 2AZ, UK

[2]School of Mathematics, University of Leeds, Leeds LS2 9JT, UK

The nonlinear stability of immiscible two–fluid Couette flows in the presence of inertia is considered. The interface between the two viscous fluids can support insoluble surfactants and the interplay between the underlying hydrodynamic instabilities and Marangoni effects is explored analytically and computationally in both two and three dimensions. Asymptotic analysis when one of the layers is thin relative to the other yields a coupled system of nonlinear equations describing the spatiotemporal evolution of the interface and its local surfactant concentration. The system is nonlocal and arises by appropriately matching solutions of the linearised Navier–Stokes equations in the thicker layer to the solution in the thin layer. The scaled models are used to study different physical mechanisms by varying the Reynolds number, the viscosity ratio between the two layers, the total amount of surfactant present initially and a scaled Péclet number measuring diffusion of surfactant along the interface. The linear stability of the underlying flow to two– and three–dimensional disturbances is investigated and a Squire's type theorem is found to hold when inertia is absent. When inertia is present, three–dimensional disturbances can be more unstable than two–dimensional ones and so Squire's theorem does not hold. The linear instabilities are followed into the nonlinear regime by solving the evolution equations numerically; this is achieved by implementing highly accurate linearly implicit schemes in time with spectral discretisations in space. Numerical experiments for finite Reynolds numbers indicate that for two–dimensional flows the solutions are mostly nonlinear travelling waves of permanent form, even though these can lose stability via Hopf bifurcations to time–periodic travelling waves. As the length of the system (that is the wavelength of periodic waves) increases, the dynamics become more complex and include time–periodic, quasi–periodic as well as chaotic fluctuations. It is also found that one–dimensional interfacial travelling waves of permanent form can become unstable to spanwise perturbations for a wide range of parameters, producing three–dimensional flows with interfacial profiles that are two–dimensional and travel in the direction of the underlying shear. Nonlinear flows are also computed for parameters which predict linear instability to three–dimensional disturbances but not two–dimensional ones. These are found to have a one–dimensional interface in a rotated frame with respect to the direction of the underlying shear and travel obliquely without changing form.

Key words: two–phase Couette flows, surfactants, Marangoni instability, secondary instability.

---

† Email address for correspondence: anna.kalogirou09@imperial.ac.uk

1. **Introduction**

A two–layer Couette flow consists of two immiscible superposed layers of different viscous fluids confined between two horizontal plates and driven by the motion of one of the walls, as shown in figure 1. An exact steady–state solution of the Navier–Stokes equations exists with a flat interface and constant but different shear supported in each fluid region. Yih (1967) first showed that the flow can be linearly unstable to long waves for all non–zero Reynolds numbers, as long as the two fluids have different viscosities. The relative thicknesses and viscosities of the undisturbed layers play a crucial role and lead to the so–called thin layer effect (other parameters such as the density ratio and the surface tension being held fixed): long waves can be stabilised by placing the less viscous fluid in a relatively thin undisturbed layer, and short waves can be stabilised by a sufficient amount of surface tension (see Joseph & Renardy (1992)).

Following Yih's seminal work, Hooper & Boyd (1983) focused on instabilities intrinsic to the interface by examining unbounded viscous two–fluid flows, and found that the flow is always unstable to short waves if surface tension is absent. In a related study, Hooper (1985) considered the semi–infinite problem (the upper wall of the channel is moved to infinity) so that the thinner layer of fluid is always at the wall. The results reveal that the flow is always linearly stable if the lower fluid is less viscous than the upper fluid, in line with the thin layer effect. Furthermore, Hooper showed that the presence of one wall causes long wavelength instabilities with higher growth rates than those found by Yih, confirming that the presence of a second wall on the flow is stabilising. The long–wave assumption was removed by Renardy (1985, 1987), who solved the linear problem numerically and determined the spectrum for arbitrary flow parameters and wavenumbers. Based on the same flow configuration used by Hooper (1985), Hooper & Boyd (1987) demonstrated that the semi–bounded problem can be destabilised by three types of instability. They discovered a new instability confined to the lower bounded layer, leaving the upper unbounded fluid relatively undisturbed. A 'phase diagram' of interfacial instabilities in two–layer Couette flows was provided by Charru & Hinch (2000). The authors also proposed a physical explanation of the instabilities arising in two–layer Couette flows. In a long–wave weakly nonlinear study that retains surface tension (it needs to be asymptotically large), Hooper & Grimshaw (1985) derived and studied a Kuramoto–Sivashinsky equation for the interface, showing that surface tension and nonlinearity saturate the inertial instability to produce non–uniform states.

The presence of insoluble surfactants in two–fluid shear flows can induce destabilising Marangoni forces. It was shown by Frenkel & Halpern (2002) and Halpern & Frenkel (2003) that surfactants can produce linear instability even at zero Reynolds number (the former paper carries out a long wavelength expansion, and the latter considers arbitrary perturbations under Stokes flow conditions). Viscosity stratification is not required (in contrast to the instability found by Yih (1967)) and the instability is switched off in the absence of shear or interfacial surfactant. Interestingly, the presence of a wall appears to be a necessary but not sufficient condition for the Marangoni instability - see the analysis discussion by Pozrikidis & Hill (2011). A recent review of Marangoni instabilities in thin films can be found in Craster & Matar (2009).

The effect of inertia on the Marangoni instability of the interface was studied numerically by Pozrikidis (2004) and by a linear stability analysis in Blyth & Pozrikidis (2004b) for arbitrary wavelength perturbations based on the Orr–Sommerfeld equation. The role of inertia was further investigated by Frenkel & Halpern (2005) for perturbations of long wavelength. The results of these papers suggest that increased inertia acts to widen the range of unstable wavenumbers, making the flow more susceptible to linear instability.

The findings of Frenkel and Halpern regarding Marangoni instability in the presence of insoluble surfactants were confirmed by Blyth & Pozrikidis (2004a). These authors also included the effect of gravity and surfactant surface diffusivity in a generalisation of the linear stability analysis to arbitrary wavenumbers. They also presented direct numerical simulations on relatively small periodic domains that reveal saturated nonlinear travelling wave solutions. We note that direct simulations on large domains that support intricate dynamics are quite challenging and hence dimensionally reduced models are very useful in mapping out the underlying nonlinear phenomena for wide parameter ranges. Additional nonlinear aspects of the flow using model equations valid when one of the fluid layers is thin relative to the other were carried out by Frenkel & Halpern (2006). The authors considered waves on longer periodic domains and presented computations that indicate the disappearance of the nonlinear travelling waves predicted by Blyth & Pozrikidis (2004a). More specifically, Frenkel & Halpern (2006) assume that the upper fluid is unbounded and derive a system of weakly nonlinear evolution equations coupling the film thickness and the local surfactant concentration in regimes where the fluid dynamics of the upper fluid do not enter into the final equations. Numerical solutions of these equations demonstrate that as the domain size is increased, the solutions become unstable to smaller wavenumber perturbations.

More recently, Bassom et al. (2010) considered the problem of two–layer Couette flows when the lower layer is thin compared to the upper layer, and derived a pair of weakly nonlinear equations describing the coupled interfacial and surfactant dynamics. The equation contains a linear nonlocal integral term (a pseudo–differential operator) which couples the film and upper fluid dynamics (such nonlocal couplings have been found in core–annular flows also, both in the absence and presence of surfactants - see Papageorgiou et al. (1990) and Kas-Danouche et al. (2009)). Numerical calculations have been carried out for a local approximation of the system (the nonlocal operator is approximated by a truncation of its long–wave expansion in Fourier space, making it a linear combination of partial derivatives) for asymptotically small and finite Reynolds numbers in the upper layer. For asymptotically small Reynolds number, finite amplitude travelling waves emerge, while periodic travelling waves, chaotic solutions and complex dynamics result in the case of order one Reynolds number. The full nonlocal system at asymptotically small Reynolds numbers was solved by Kalogirou et al. (2012), who found intricate dynamical phenomena (quasi–periodicity, chaos) that have not been explored in Bassom et al. (2010) (the authors showed travelling wave solutions only). Furthermore, Kalogirou et al. (2012) compared local and nonlocal computations with a good agreement. The present study is devoted to the nonlinear dynamics of the problem at order one Reynolds numbers via a systematic analytical and computational study of the full nonlocal equations. A more recent study by Samanta (2013) considers the linear problem governed by an Orr–Sommerfeld system, along with model equations derived using depth–averaging methods; our study is quite distinct from this since we consider the nonlocal coupling between a thin fluid layer with another layer of order–one thickness. The innovation of this work also lies in the study of the stability of three–dimensional flows via investigation of validity of a Squire's type theorem. The stability in three–dimensions of the nonlinear travelling wave solutions observed in the two–dimensional flow is also examined.

The structure of the paper is as follows. §2 provides the governing equations and boundary conditions, while in §3 the derivation of the underlying evolution equations is briefly described. In §4 we provide the linear stability properties of the system and prove a Squire's type theorem in the absence of inertia. We then present numerical solutions obtained by solving initial value problems; we first pursue a detailed numerical study of the two–dimensional flow in §5, and then study the stability of one–dimensional interfacial
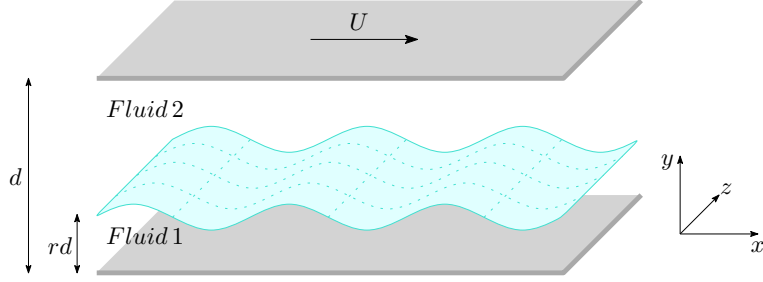
FIGURE 1. Geometry of the problem: two superposed fluids in a channel, driven by the motion of the upper wall with horizontal speed U. The walls are separated by a distance d and the flat interface is located at rd. The wavy surface represents the disturbed interface.

travelling wave solutions to spanwise perturbations in §6. We conclude by discussing our results in §7.

2. Governing equations

Consider the flow of two immiscible, incompressible viscous fluids of equal density ρ in a channel of height d, driven by the motion of the upper plate with velocity U - see figure 1. Using cartesian coordinates, the walls are at $y = 0$ and $y = d$, the lower fluid 1 occupies $0 < y < S(x, z, t)$ and the upper fluid 2 lies in the region $S(x, z, t) < y < d$; $y = S(x, z, t)$ is the position of the interface between the fluids and t is time. The fluids have unequal viscosities μ_1 and μ_2, and an insoluble surfactant with local concentration $\Gamma(x, z, t)$ is present on the interface and acts to lower the interfacial tension γ. In the undisturbed state the interface is assumed to be at $y = rd$, where $0 < r < 1$ is a constant.

We non–dimensionalise lengths with d, velocities with U, pressures with ρU^2, time with d/U, surface tension by its clean value γ_c and the surfactant concentration by the maximum packing value Γ_∞. The Navier–Stokes equations in each phase $i = 1, 2$ are

$$\frac{\partial \boldsymbol{u}_i}{\partial t} + \boldsymbol{u}_i \cdot \nabla \boldsymbol{u}_i = -\nabla p_i + \frac{1}{Re_i} \nabla^2 \boldsymbol{u}_i, \tag{2.1a}$$

$$\nabla \cdot \boldsymbol{u}_i = 0, \tag{2.1b}$$

where $\boldsymbol{u}_i = (u_i, v_i, w_i)^T$ is the velocity field and Re_i are the Reynolds numbers in each fluid

$$Re_1 = \frac{\rho U d}{\mu_1}, \quad Re_2 = \frac{\rho U d}{\mu_2} = \frac{Re_1}{m}, \tag{2.2}$$

with $m = \mu_2/\mu_1$ the viscosity ratio. In addition to the no–slip conditions at the walls

$$u_1 = v_1 = w_1 = 0 \quad \text{at} \quad y = 0, \tag{2.3a}$$

$$u_2 = 1, \ v_2 = w_2 = 0 \quad \text{at} \quad y = 1, \tag{2.3b}$$

there are several boundary conditions to be imposed at the interface $y = S(x, z, t)$. These are continuity of velocities

$$u_1 = u_2, \ v_1 = v_2, \ w_1 = w_2 \quad \text{at} \quad y = S(x, z, t), \tag{2.4a}$$

a kinematic condition

$$v_i = S_t + u_i S_x + w_i S_z, \quad i = 1, 2, \tag{2.5}$$

and continuity of normal and tangential stresses

$$
\left[-p_i \left(1 + S_x^2 + S_z^2 \right) + \frac{2}{Re_i} \left(S_x^2 u_{ix} + S_z^2 w_{iz} + v_{iy} - S_x \left(u_{iy} + v_{ix} \right) - S_z \left(v_{iz} + w_{iy} \right) \right. \right.
$$
$$
\left. \left. + S_x S_z \left(u_{iz} + w_{ix} \right) \right) \right]_2^1 = \frac{(1 - \beta \Gamma)}{We} \left(\frac{\left(1 + S_x^2 \right) S_{zz} - 2 S_x S_z S_{xz} + \left(1 + S_z^2 \right) S_{xx}}{\sqrt{1 + S_x^2 + S_z^2}} \right),
$$
$$(2.6a)$$

$$
\left[m_i \left(2 S_x \left(u_{ix} - v_{iy} \right) + S_z \left(u_{iz} + w_{ix} \right) + S_x S_z \left(v_{iz} - w_{iy} \right) + \left(S_x^2 - 1 \right) \left(u_{iy} + v_{ix} \right) \right) \right]_2^1
$$
$$
= Ma \, \Gamma_x \sqrt{1 + S_x^2 + S_z^2},
$$
$$(2.6b)$$

$$
\left[m_i \left(2 S_z \left(w_{iz} - v_{iy} \right) + S_x \left(u_{iz} + w_{ix} \right) + S_x S_z \left(u_{iy} + v_{ix} \right) + \left(S_z^2 - 1 \right) \left(v_{iz} + w_{iy} \right) \right) \right]_2^1
$$
$$
= Ma \, \Gamma_z \sqrt{1 + S_x^2 + S_z^2},
$$
$$(2.6c)$$

where the jump notation $[f_i]_2^1 = f_1 - f_2$ is used. Here, $m_1 = 1$, $m_2 = m$, $We = \frac{\rho U^2 d}{\gamma_c}$ is the Weber number, $Ma = \frac{\beta}{Ca}$ is the Marangoni number with $Ca = \frac{\mu_1 U}{\gamma_c}$ the Capillary number. The terms Γ_x and Γ_z in (2.6b) and (2.6c), respectively, are the Marangoni forces arising from variations in the surface tension and play an important role in the dynamics. In deriving (2.6), we have assumed an equation of state $\gamma = \gamma(\Gamma)$ for the dimensionless surface tension in terms of the local surfactant concentration - see Frumkin & Levich (1947), Levich (1962), Edwards et al. (1991). When surfactant is present in dilute concentrations, a linear Gibbs' isotherm can be used of the form

$$
\gamma = 1 - \beta \Gamma, \tag{2.7}
$$

where $\beta = \frac{RT\Gamma_\infty}{\gamma_c}$ is a parameter that measures the sensitivity of interfacial tension to changes in the surfactant concentration, R is the universal gas constant and T is the absolute temperature. Note that in the weakly nonlinear analysis that follows the use of (2.7) is fully justified. Finally, we require a conservation equation for Γ and this reads (Li & Pozrikidis 1997; Stone & Leal 1990; Wong et al. 1996)

$$
\frac{\partial \Gamma}{\partial t} - \frac{S_t}{(1 + S_x^2 + S_z^2)} (\Gamma_x S_x + \Gamma_z S_z)
$$
$$
+ \frac{1}{\sqrt{1 + S_x^2 + S_z^2}} \left[\frac{\partial}{\partial x} \left(\sqrt{1 + S_x^2 + S_z^2} \, u^1 \Gamma \right) + \frac{\partial}{\partial z} \left(\sqrt{1 + S_x^2 + S_z^2} \, u^2 \Gamma \right) \right]
$$
$$
+ \frac{\Gamma \left(u_I S_x - v_I + w_I S_z \right)}{\sqrt{1 + S_x^2 + S_z^2}} \left(\frac{\left(1 + S_x^2 \right) S_{zz} - 2 S_x S_z S_{xz} + \left(1 + S_z^2 \right) S_{xx}}{\sqrt{1 + S_x^2 + S_z^2}} \right)
$$
$$
- \frac{1}{Pe} \frac{1}{\sqrt{1 + S_x^2 + S_z^2}} \left[\frac{\partial}{\partial x} \left(\frac{\Gamma_x (1 + S_z^2) - \Gamma_z S_x S_z}{\sqrt{1 + S_x^2 + S_z^2}} \right) + \frac{\partial}{\partial z} \left(\frac{\Gamma_z (1 + S_x^2) - \Gamma_x S_x S_z}{\sqrt{1 + S_x^2 + S_z^2}} \right) \right]
$$
$$
= 0, \tag{2.8}
$$

where

$$u^1 = \frac{(u_\mathrm{I} + v_\mathrm{I} S_x)(1 + S_z^2) - (v_I S_z + w_\mathrm{I}) S_x S_z}{1 + S_x^2 + S_z^2}, \qquad (2.9)$$

$$u^2 = \frac{(v_\mathrm{I} S_z + w_\mathrm{I})(1 + S_x^2) - (u_\mathrm{I} + v_\mathrm{I} S_x) S_x S_z}{1 + S_x^2 + S_z^2},$$

and u_I, v_I, w_I are the velocities at the interface. Here, $Pe = \frac{Ud}{D_s}$ is the Péclet number for constant surfactant diffusivity D_s.

The system of equations and boundary conditions (2.1)–(2.8) admits an exact parallel flow solution $\boldsymbol{u}_1 = (\overline{U}_1(y), 0, 0)$, $\boldsymbol{u}_2 = (\overline{U}_2(y), 0, 0)$, with a flat interface at $y = r$ (without loss of generality, $\overline{P}_1 = \overline{P}_2 = 0$). The solution is

$$\overline{U}_1 = \frac{my}{r(m-1)+1}, \quad \overline{U}_2 = \frac{y + r(m-1)}{r(m-1)+1}. \qquad (2.10)$$

In what follows, we make analytical progress by developing a weakly nonlinear theory when one of the fluid layers is thin relative to the channel thickness. We describe an asymptotic theory that retains the effect of inertia in the thicker layer in order to generate dynamics that extend beyond the reach of usual lubrication theories. The resulting equations are found to be useful in describing interfacial shapes observed in experiments and this study is currently under way.

3. Derivation of the evolution equations

A detailed derivation of the evolution equations in the two–dimensional flow case was presented by Bassom et al. (2010), where the equations were analysed in the special limit of localising nonlocal operators in Fourier space. Our objective here is to solve the full equations and study the stability of solutions to spanwise perturbations. Hence, a brief sketch of the derivation based on a three–dimensional flow configuration is included for completeness.

The lower layer is assumed thin and has undisturbed thickness $r = \epsilon \ll 1$. Interfacial and surfactant perturbations are introduced by $S(x, z, t) = \epsilon + \delta_1(\epsilon) H(x, z, t)$, $\Gamma(x, z, t) = \Gamma_0 + \delta_2(\epsilon) \Gamma'(x, z, t)$, with $\delta_1(\epsilon)$, $\delta_2(\epsilon) \ll 1$ selected to ensure coupling between the two layers and the presence of Marangoni forces at leading order. The scalings of Kas-Danouche et al. (2009) (also adopted by Bassom et al. (2010)) follow,

$$\delta_1 = \epsilon^2, \quad \Gamma_0 = \delta_2 \Gamma_0', \quad Ca = \epsilon Ca_0, \quad Ma = \epsilon^2 \delta_2^{-1} Ma_0, \quad Pe = \epsilon^{-2} Pe_0, \qquad (3.1)$$

where Γ_0', Ca_0, Ma_0, Pe_0 are of $O(1)$, while δ_2 is not given a canonical scaling; it is sufficient to have $\delta_2 \to 0$ as $\epsilon \to 0$. The surfactant concentration scaling corresponds to the dilute limit and allows Marangoni forces to influence the nonlinear dynamics (otherwise linear dynamics ensue - Wei (2005)). It follows, then, that $\Gamma(x, z, t) = \delta_2 \tilde{\Gamma}(x, z, t)$ where $\tilde{\Gamma}(x, z, t) = \Gamma_0' + \Gamma'$, and this will be used as a dependent variable in the sequel. Introducing a stretched variable $\zeta = y/\epsilon$ in region 1 (the undisturbed interface is at $\zeta = 1$), we expand variables there as $u_1 = \overline{U}_1(y) + \epsilon^3 U_1(x, \zeta, z, t) + \cdots$, $v_1 = \epsilon^4 V_1(x, \zeta, z, t) + \cdots$, $w_1 = \epsilon^3 W_1(x, \zeta, z, t) + \cdots$, $p_1 = \epsilon P_1(x, \zeta, z, t) + \cdots$, while in region 2 we write $u_2 = \overline{U}_2(y) + \epsilon^2 U_2(x, y, z, t) + \cdots$, $v_2 = \epsilon^2 V_2(x, y, z, t) + \cdots$, $w_2 = \epsilon^2 W_2(x, y, z, t) + \cdots$, $p_2 = \epsilon^2 P_2(x, y, z, t) + \cdots$. These expansions are motivated by requiring a leading order balance between the pressure gradient and viscous terms in the momentum equations, and continuity of velocities at the perturbed interface. Substituting these expansions into the Navier–Stokes equations (2.1) and the normal and tangential stress balances (2.6),

yields to leading order

$$V_1\big|_{\zeta=1} = -\frac{1}{3Ca_0}\left(H_{xxxx} + 2H_{xxzz} + H_{zzzz}\right) + \frac{Ma_0}{2}\left(\Gamma'_{xx} + \Gamma'_{zz}\right) - \frac{m}{2}T\big|_{y=0}, \quad (3.2)$$

where $T(x,y,z) = U_{2xy} + V_{2xx} + V_{2zz} + W_{2zy}$ is found by solving the problem in the upper layer. Introducing the Galilean transformation $\tilde{x} = x - \overline{U}_1(\epsilon)t$ and the slow time scale $\tilde{t} = \epsilon^2 t$, casts the kinematic condition (2.5) into

$$H_{\tilde{t}} + mHH_{\tilde{x}} = V_1\big|_{\zeta=1}, \quad (3.3)$$

while using the same transformations in the surfactant equation (2.8) yields at leading order

$$\tilde{\Gamma}_{\tilde{t}} + m\left(H\tilde{\Gamma}\right)_{\tilde{x}} = \frac{1}{Pe_0}\left(\tilde{\Gamma}_{\tilde{x}\tilde{x}} + \tilde{\Gamma}_{zz}\right). \quad (3.4)$$

Coupling between the layers takes place through $T\big|_{y=0}$ which depends on the size of the Reynolds number in the upper layer. Inertia enters when $Re_2 = O(1)$ and in what follows we use R_e in place of Re_2. A linearised Navier–Stokes system results at leading order; transformation into Fourier space, use of the function $f = -\frac{\partial \hat{V}_2}{\partial y}$ (hat denotes Fourier transform) and elimination of the pressure, provides

$$\left(\frac{\partial^4 \hat{V}_2}{\partial y^4} - 2\left(k_1^2 + k_2^2\right)\frac{\partial^2 \hat{V}_2}{\partial y^2} + \left(k_1^2 + k_2^2\right)^2 \hat{V}_2\right) - ik_1 R_e\, y\left(\frac{\partial^2 \hat{V}_2}{\partial y^2} - \left(k_1^2 + k_2^2\right)\hat{V}_2\right) = 0, \quad (3.5)$$

which is an Orr–Sommerfeld type equation. The boundary conditions are

$$\hat{V}_2 = 0,\ \hat{V}_{2y} = 0 \quad \text{at} \quad y = 1, \quad (3.6)$$
$$\hat{V}_2 = 0,\ \hat{V}_{2y} = -ik_1(m-1)\hat{H} \quad \text{at} \quad y = 0,$$

and represent no–slip at the upper wall and continuity of velocities at the interface. Writing $\hat{V}_2 = -ik_1(m-1)\hat{H}F(y)$, yields the following normalised boundary value problem for $F(y)$

$$\left(F'''' - 2k^2 F'' + k^4 F\right) - ik_1 R_e\, y\left(F'' - k^2 F\right) = 0, \quad (3.7a)$$

$$F(0) = 0,\ F'(0) = 1, \quad F(1) = 0,\ F'(1) = 0, \quad (3.7b)$$

with $k = \sqrt{k_1^2 + k_2^2}$. Even though a solution can be written in terms of Airy functions and their integrals (see for example Hooper & Boyd (1983) and Kalogirou (2014)), it is much more straightforward to obtain numerical solutions directly; this is achieved here using a finite difference method. Once $F(y; k_1, k_2)$ is known, we can take inverse transforms to readily obtain

$$T\big|_{y=0} = \frac{i}{2\pi^2}(1-m)\int_{-\infty}^{+\infty}\int_{-\infty}^{+\infty}\mathcal{N}(k_1,k_2)\hat{H}(k_1,k_2)e^{i(k_1 x + k_2 z)}\,dk_1 dk_2, \quad (3.8)$$

where

$$\mathcal{N}(k_1,k_2) = -\frac{k_1}{2}F''(0). \quad (3.9)$$

With $T\big|_{y=0}$ known in terms of the interfacial shape H, equation (3.2) is then used in the kinematic equation (3.3), which along with the surfactant transport equation (3.4) provide the following system (with a canonical rescaling applied and the tildes dropped

from all terms)

$$H_t + HH_x + \nabla^4 H + \frac{i\Lambda}{4\pi^2} \int_{-\infty}^{+\infty} \int_{-\infty}^{+\infty} \mathcal{N}(k_1, k_2)\hat{H}(k_1, k_2)\mathrm{e}^{ik_1 x + ik_2 z} \,\mathrm{d}k_1 \mathrm{d}k_2 - \nabla^2 \Gamma = 0,$$
(3.10)

$$\Gamma_t + (H\Gamma)_x - \eta\nabla^2\Gamma = 0. \tag{3.11}$$

The parameters Λ and $\eta > 0$ represent viscosity stratification effects and surfactant diffusivity, respectively, and are given by

$$\Lambda = 3Ca_0\, m(1-m), \quad \eta = \frac{3Ca_0}{Pe_0}. \tag{3.12}$$

Note that Λ is positive if $m < 1$, i.e. when the film is more viscous than the upper layer fluid, and negative otherwise.

For ease of representation, the nonlocal term was developed using Fourier transforms; nevertheless, the problem is more appropriately defined on finite domains (typically periodic of size $2L_x \times 2L_z$, say), so a Fourier series representation will be used - see §5.1. The nonlinear system (3.10)–(3.11) retains three important physical mechanisms that we wish to study in detail: shear–induced instabilities through the Λ term; Marangoni effects through the $\nabla^2\Gamma$ term in (3.10); short–wave surface tension stabilisation through the $\nabla^4 H$ term in (3.10).

Considering the two–dimensional problem, i.e. setting $\partial_z = 0$, $k_2 = 0$ (and $k_1 = k$), the set of equations (3.10)–(3.11) is simplified by

$$H_t + HH_x + H_{xxxx} + \frac{i\Lambda}{2\pi} \int_{-\infty}^{+\infty} \mathcal{N}(k)\hat{H}(k)\mathrm{e}^{ikx} \,\mathrm{d}k - \Gamma_{xx} = 0, \tag{3.13}$$

$$\Gamma_t + (H\Gamma)_x - \eta\Gamma_{xx} = 0. \tag{3.14}$$

Extensive numerical computations on the above one–dimensional system were carried and presented in a later section.

4. Linear stability analysis

We now consider the linear stability properties of the system (3.10)–(3.11). Linearising about the base state $H = 0$, $\Gamma = \Gamma_0$ and looking for normal mode solutions proportional to $\mathrm{e}^{ik_1 x + ik_2 z + \sigma t}$, where k_1, k_2 are real wavenumbers in $x-$ and $z-$directions respectively, yields the following dispersion relation for the growth rate $\sigma(k_1, k_2)$

$$\sigma^2 + \left(k^4 + i\Lambda\mathcal{N}(k_1, k_2) + \eta k^2\right)\sigma + \left(\eta k^6 + i\eta\Lambda\mathcal{N}(k_1, k_2)k^2 - i\Gamma_0 k_1 k^2\right) = 0, \tag{4.1}$$

where $k = \sqrt{k_1^2 + k_2^2}$. There are two modes with growth rates

$$\sigma_{1,2} = -\frac{k^4 + i\Lambda\mathcal{N}(k_1, k_2) + \eta k^2}{2} \pm \frac{1}{2}\sqrt{(k^4 + i\Lambda\mathcal{N}(k_1, k_2) - \eta k^2)^2 + 4i\Gamma_0 k_1 k^2}, \tag{4.2}$$

where the plus sign corresponds to σ_1 and the minus sign to σ_2; instability is possible if the real part of σ_1 or σ_2 is positive, i.e. if $s_{1,2} = \mathrm{Re}(\sigma_{1,2}) > 0$. For equal–viscosity fluids characterised by $\Lambda = 0$, the growth rates in the long–wave regime $k_1, k_2 \ll 1$ are

$$s_{1,2} = \pm\sqrt{\frac{\Gamma_0}{2}}\, k_1^{1/2}\, k - \frac{\eta}{2}k^2 + \cdots, \tag{4.3}$$

thus the flow can be unstable in this case but only in the presence of surfactant, i.e. for $\Gamma_0 \neq 0$. On the contrary, for $\Lambda \neq 0$ and $k \ll 1$, substitution of a localisation of $\mathcal{N}(k_1, k_2)$
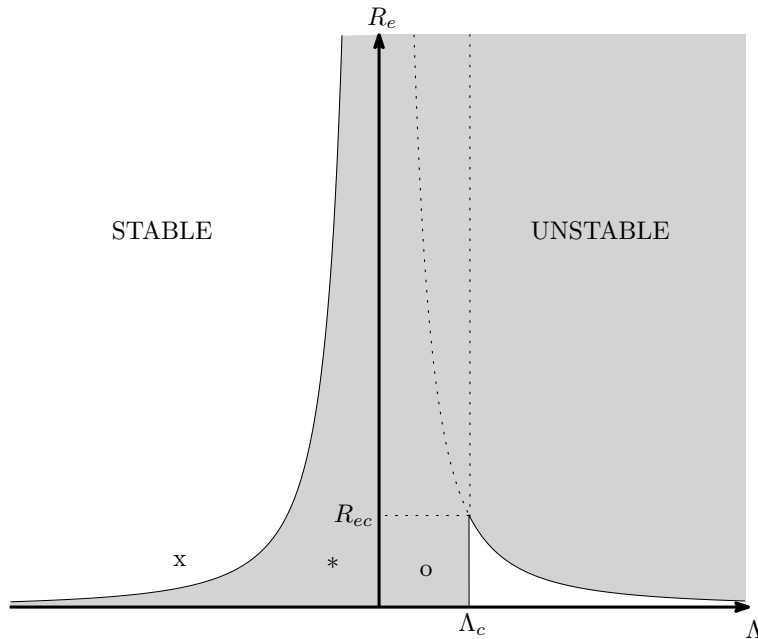
FIGURE 2. Stability diagram corresponding to two–dimensional flows, showing regions of stability (white) and instability (grey) in the $\Lambda - R_e$ parameter space. The critical points are $\Lambda_c = \Gamma_0/2\eta$ and $R_{ec} = 30\Gamma_0/\Lambda_c^2 = 120\eta^2/\Gamma_0$.

(see Appendix A for details) into the dispersion relation yields

$$s_1 = \frac{(\Gamma_0 - 2\eta\Lambda)}{2\Lambda}k^2 + \mathcal{O}(k^3), \qquad s_2 = \frac{(R_e\Lambda^2 - 30\Gamma_0)}{60\Lambda}k_1^2 - \frac{\Gamma_0}{2\Lambda}k_2^2 + \mathcal{O}(k^3). \qquad (4.4)$$

4.1. *Two–dimensional perturbations*

For two–dimensional perturbations, the growth rates are obtained by setting $k_2 = 0$ in (4.3) and (4.4) and are identical to the ones found by Bassom et al. (2010) and reduce to the ones derived by Frenkel & Halpern (2002) and Wei (2005) in appropriate limits. A stability diagram showing neutral curves in $\Lambda - R_e$ parameter space is given in figure 2. Instability regions are shaded while the flow is linearly stable in the unshaded regions. One observation from the diagram is that instability always exists for $\Lambda = 0$ at any Reynolds number, in complete agreement with the findings of Frenkel & Halpern (2002) and Halpern & Frenkel (2003), who found that Marangoni instability exists even for fluids with equal viscosities. Moreover, increasing $\Lambda > 0$ destabilises the flow above the critical value $(30\Gamma_0/R_e)^{1/2}$ (i.e. beyond the curve $R_e\Lambda^2 = 30\Gamma_0$). Decreasing $\Lambda < 0$ leads to the opposite effect; this suggests a viscosity stratification stabilisation of the Marangoni instability, as found by Kalogirou et al. (2012). Note that in the absence of surfactants (this corresponds to infinite surfactant diffusivity $\eta \to \infty$ and $\Gamma_0 = 0$), the curves in figure 2 shrink to zero and the line $\Lambda = \Lambda_c$ coincides with the $\Lambda = 0$ axis. In this case, the only unstable region is the first quadrant $\Lambda > 0$, $R_e > 0$. This is consistent with stability results for two–layer Couette flows without surfactants - it is known that the flow is linearly unstable if $\Lambda > 0$ and $R_e > 0$, while the flow is stable for $\Lambda < 0$ at any Reynolds number, in agreement with the results of Yih (1967) and Hooper (1985).

Another remark is that for $R_e = 0$ the flow is unstable as long as Λ remains smaller than the critical value $\Lambda_c = \Gamma_0/2\eta$, as found by Kalogirou et al. (2012). An increase in
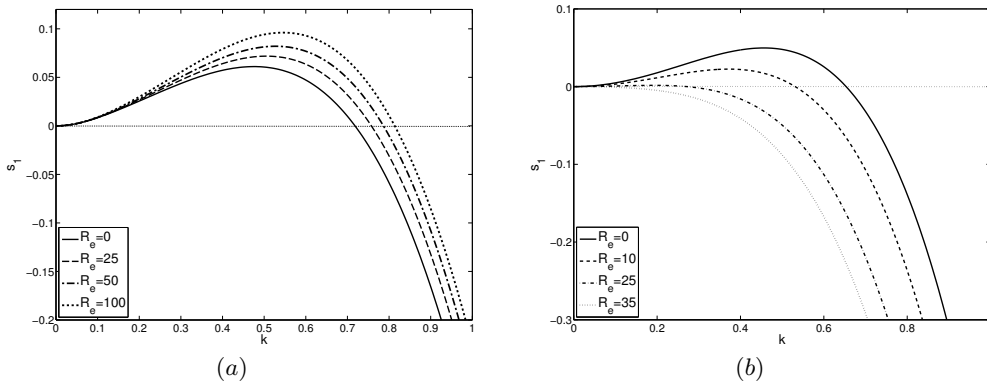
FIGURE 3. Effect of the Reynolds number on unstable growth rates of two–dimensional flows, for $\Gamma_0 = 1$, $\eta = 1$. (a) Positive $\Lambda = 0.25$: increasing $R_e = 0, 25, 50, 100$ leads to larger unstable region. (b) Negative $\Lambda = -1.0$: increasing $R_e = 0, 10, 25, 35$ shrinks the unstable region and eventually stabilises the problem above a cut–off Reynolds number value.

the Reynolds number stabilises the flow if $\Lambda < 0$ and destabilises the flow if $\Lambda > 0$. This result is consistent with previous studies that demonstrate that inertial effects increase the growth of the Marangoni instability to produce new regions of instability, as long as the film is more viscous than the overlying fluid (Pozrikidis 2004; Blyth & Pozrikidis 2004b; Frenkel & Halpern 2005). This is also confirmed by figure 3(a) for the unstable case $\Lambda = 0.25$, $\Gamma_0 = 1$, $\eta = 1$, where the growth rates are shown as functions of the wavenumber for $R_e = 0, 25, 50, 100$. The cut–off wavenumbers below which the flow becomes stable are $k_c = 0.718, 0.758, 0.787, 0.814$, respectively, showing that increasing inertia enhances the already present Marangoni instability, as expected. The short–wave stabilisation is due to surface tension effects (Hooper & Boyd 1983), represented by the H_{xxxx} term in the evolution equation for the film thickness (note that the large k behaviour of $\mathcal{N}(k) \sim k^2$ (Kalogirou 2014) is subdominant relative to that of H_{xxxx}). If the film is less viscous than the upper fluid, inertial effects cause stabilisation of long waves. Growth rates for $\Lambda = -1.0$, $\Gamma_0 = 1$, $\eta = 1$ at different R_e are given in figure 3(b), and it is seen that the growth rates decrease with increasing Reynolds numbers.

4.2. *Three–dimensional perturbations*

In the case of three–dimensional disturbances, a sufficient condition for instability follows if one of the growth rates in the long–wave approximations (4.4) is positive. We will discuss the cases $\Lambda > 0$ and $\Lambda < 0$ separately.

In the case of a more viscous film ($\Lambda > 0$), this is true if

$$\Gamma_0 - 2\eta\Lambda > 0 \qquad \text{or} \qquad R_e\Lambda^2 - 30\Gamma_0 > 0. \qquad (4.5)$$

The first of conditions (4.5) can be satisfied in one of three physical ways: by either having a sufficiently large initial surfactant concentration Γ_0, a sufficiently small surfactant diffusion coefficient η, or by decreasing the viscosity difference between the two fluids so that Λ is small. The second condition in (4.5) is physically possible by either imposing a considerable viscosity contrast between the two fluids (i.e. Λ large), by having a sufficiently large Reynolds number, or by having a small initial surfactant concentration Γ_0. Note that for three–dimensional perturbations the two neutral stability hyperbolae in figure 2 (defined by $R_e = \frac{30\Gamma_0}{\Lambda^2}$ in the figure), become $R_e = \frac{30\Gamma_0}{\Lambda^2}\left(1 + \frac{k_2^2}{k_1^2}\right)$. For non–zero values of k_2 these curves shift upwards (compared to the original curves that correspond
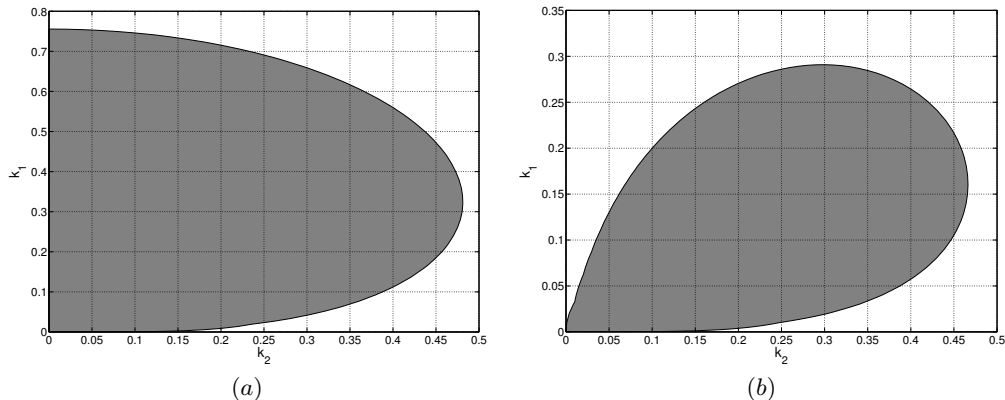
FIGURE 4. Unstable growth rates of three–dimensional flows, showing regions of instability (grey) and stability (white) against k_1, k_2 for $\Gamma_0 = 1$, $\eta = 1$. (a) $Re = 25$, $\Lambda = 0.25$, corresponding to the unstable point 'o' on the stability diagram in figure 2. (b) $Re = 35$, $\Lambda = -1.0$, corresponding to the stable point 'x' on the stability diagram in figure 2.

to $k_2 = 0$), implying that for $\Lambda > 0$ three–dimensional perturbations are more stable than two–dimensional ones. This result is also present in figure 4(a), where the instability region is shown in the $k_1 - k_2$ space for $Re = 25$, $\Lambda = 0.25$, $\Gamma_0 = 1$, $\eta = 1$; we have established (data not shown) that the maximum growth occurs on the axis $k_2 = 0$.

On the other hand, for $\Lambda < 0$ this shift of the stability curves increases the region of instability, causing regions corresponding to two–dimensional stability in $\Lambda - R_e$ space (unshaded regions in figure 2) to move into the unstable grey shaded region. In particular, the point marked 'x' in figure 2 will now fall into the unstable region and this is also confirmed in figure 4(b), where the region of instability is portrayed for $Re = 35$, $\Lambda = -1.0$, $\Gamma_0 = 1$, $\eta = 1$. The choice of parameter values is such that the corresponding two–dimensional perturbations are stable (in particular, they are stable for any $R_e > 30$), and this is also seen from figure 4(b) where the instability region does not include the axis $k_2 = 0$.

The above results motivate the investigation of the validity of a Squire's type theorem in two–layer parallel flows with surfactants. In the absence of surfactants, it is known that if a three–dimensional perturbation is unstable, then a two–dimensional perturbation having the same flow parameters exists and is more unstable (Hesla et al. 1986). As discussed in the previous paragraph, for order one Reynolds numbers there exist three–dimensional perturbations that are more unstable than two–dimensional ones, hence Squire's theorem cannot hold. The theorem holds for zero Reynolds number, however, as shown below - an alternative derivation can be found in Halpern & Frenkel (2003). The dispersion relation (4.1) with $Re = 0$ and use of the local system expansions (see Appendix A), becomes

$$\sigma^2 + p_1(k_1, k_2)\sigma + p_0(k_1, k_2) = 0, \tag{4.6}$$

where $p_0(k_1, k_2)$, $p_1(k_1, k_2)$ are polynomials. Denote the positive growth rate by σ_1, i.e.

$$\sigma_1 = -\frac{p_1}{2} + \frac{\sqrt{p_1^2 - 4p_0}}{2}. \tag{4.7}$$

The goal is to find the critical point (k_1^*, k_2^*) where σ_1 has a local (and global) maximum.

This can be done by finding the values (k_1^*, k_2^*) where

$$\frac{\partial \sigma_1}{\partial k_1} = 0, \quad \frac{\partial \sigma_1}{\partial k_2} = 0 \qquad \text{and} \qquad \frac{\partial^2 \sigma_1}{\partial k_1^2} \frac{\partial^2 \sigma_1}{\partial k_2^2} - \frac{\partial^2 \sigma_1}{\partial k_1 k_2} > 0, \quad \frac{\partial^2 \sigma_1}{\partial k_1^2} < 0. \quad (4.8)$$

It can be shown that $\frac{\partial \sigma_1}{\partial k_2} = 0$ if and only if $k_2 = 0$; moreover, $\frac{\partial \sigma_1}{\partial k_1} = 0$ for a $k_1^* \neq 0$. At the point $(k_1^*, 0)$, the second derivative criteria in (4.8) also hold, thus σ_1 has its only maximum there and its real part $s_1 = \Re(\sigma_1)$ is a maximum at the same point. As an example, in the case $\Lambda = 0.25$, $\Gamma_0 = 1$, $\eta = 1$, the critical point is $(k_1^*, k_2^*) \approx (0.4757, 0)$. Hence perturbations having $k_2 = 0$ are more unstable as shown analytically - calculations using the full dispersion relation also confirm this result. In closing, we note that at zero Reynolds number the maximum growth rate is attained at $k_2 = 0$, while for order one Reynolds numbers σ_1 attains its maximum at wavenumbers $(k_1^*, k_2^*) \neq (0, 0)$.

5. Numerical solutions of the evolution equations

5.1. *Numerical Methods*

The governing equations (3.10)–(3.11) are posed on $2L_x \times 2L_z-$periodic domains. We begin by rescaling the evolution equations into the canonical domain $[0, 2\pi] \times [0, 2\pi]$ by applying the following transformations

$$x \to \frac{L_x}{\pi} x, \quad z \to \frac{L_z}{\pi} z, \quad t \to \left(\frac{L_x}{\pi}\right)^2 t, \quad H \to \frac{\pi}{L_x} H, \quad \Gamma \to \frac{\pi}{L_x} \Gamma. \quad (5.1)$$

On $2\pi \times 2\pi-$periodic domains, the nonlocal term in (3.10), which from now on will be denoted by $\mathcal{P}H$, can be expressed as the following Fourier series

$$\mathcal{P}H = \frac{i\Lambda}{\nu_1} \sum_{k_1=-\infty}^{+\infty} \sum_{k_2=-\infty}^{+\infty} \mathcal{N}(k_1\sqrt{\nu_1}, k_2\sqrt{\nu_2}) \, \widehat{H}(k_1, k_2) \, e^{ik_1 x + ik_2 z}, \quad (5.2)$$

where

$$\widehat{H}(k_1, k_2) = \frac{1}{(2\pi)^2} \int_0^{2\pi} \int_0^{2\pi} H(\xi, \zeta, t) \, e^{-ik_1 \xi - ik_2 \zeta} \, d\xi d\zeta, \quad (5.3)$$

are the Fourier coefficients of $H(x, z, t)$ and ν_1, ν_2 are new bifurcation parameters given by

$$\nu_1 = \left(\frac{\pi}{L_x}\right)^2, \quad \nu_2 = \left(\frac{\pi}{L_z}\right)^2. \quad (5.4)$$

The parameters ν_1, ν_2 (called 'viscosity' parameters in the literature), decrease as the streamwise and lateral lengths of the system L_x, L_z increase, and more linearly unstable modes enter into the dynamics. The transformed two–dimensional equations (corresponding to three–dimensional flows) become

$$H_t + HH_x + \left(\nu_1 H_{xxxx} + 2\nu_2 H_{xxzz} + \frac{\nu_2^2}{\nu_1} H_{zzzz}\right) + \mathcal{P}H - \left(\Gamma_{xx} + \frac{\nu_2}{\nu_1}\Gamma_{zz}\right) = 0, \quad (5.5)$$

$$\Gamma_t + (H\Gamma)_x - \eta\left(\Gamma_{xx} + \frac{\nu_2}{\nu_1}\Gamma_{zz}\right) = 0, \quad (5.6)$$

with $\mathcal{P}H$ given by (5.2). The corresponding one–dimensional system (for two–dimensional perturbations) becomes

$$H_t + HH_x + \nu H_{xxxx} + \frac{i\Lambda}{\nu} \sum_{k=-\infty}^{+\infty} \mathcal{N}(k\sqrt{\nu})\,\hat{H}(k)\,\mathrm{e}^{ikx} - \Gamma_{xx} = 0, \qquad (5.7)$$

$$\Gamma_t + (H\Gamma)_x - \eta\Gamma_{xx} = 0, \qquad (5.8)$$

where $\nu = (\frac{\pi}{L})^2$.

The systems (5.5)–(5.6) and (5.7)–(5.8) are discretised in space using spectral methods and in time by implicit–explicit BDF (Backward Differentiation Formula) schemes with as much as sixth order accuracy where desired - see Akrivis et al. (2015). All the results reported here were obtained using a second–order BDF scheme; for completeness, details of the scheme and its implementation for system (5.7)–(5.8) can be found in Appendix B. It is straightforward to generalise the method to system (5.5)–(5.6).

5.2. *Computational study for two–dimensional flows*

This section presents results from a large number of numerical experiments that aim to elucidate the nonlinear dynamics of the one–dimensional system (5.7)–(5.8). We use several computational diagnostic tools to monitor and identify the different attractors obtained numerically. The use of such tools is essential, mainly due to the complexity of the dynamics, non–uniqueness of solutions and large number of bifurcations (for example, we wish to be able to identify whether a solution is chaotic or quasi–periodic in time). One useful tool is the energy $E(t)$ of the solution $H(x,t)$, defined by the L_2-norm

$$E(t) := ||H(\cdot,t)||_2^2 = \int_0^{2\pi} H^2(x,t)\,\mathrm{d}x. \qquad (5.9)$$

The quadrature is performed with spectral accuracy (either using Parseval's identity or trapezoidal quadrature), and $E(t)$ can be used in highly accurate phase–plane constructions $(E(t), \dot{E}(t))$ and Poincaré maps (or return maps) satisfying $\dot{E}(t) = 0$. Such data analyses are useful in characterising the dynamical behaviour of the system as seen later. To uniformly maintain accuracy, the calculation of $\dot{E}(t)$ also needs to be carried out with spectral accuracy (a low–order finite difference formula in time is not good enough). We achieve this by multiplying (5.7) by H and integrating over a period, to find

$$\dot{E}(t) = -2\nu||H_{xx}||_2^2 - 2\int_0^{2\pi} H\,(\mathcal{P}H)\,\mathrm{d}x + 2\int_0^{2\pi} H\Gamma_{xx}\,\mathrm{d}x. \qquad (5.10)$$

All integrals on the right–hand side of (5.10) can be computed with spectral accuracy once the Fourier coefficients of H and Γ are found. Next, the values of the minima (and maxima) of the energy $E(t)$ and the times of their occurrence are estimated from the discrete time series using a second–order polynomial interpolation in time. Denoting the minima (maxima) by the set E_n, $n = 1, 2, \ldots$, we construct return maps by plotting the points (E_n, E_{n+1}), $n = 1, 2, \ldots$, in the plane. The resulting geometrical object provides information about the attractor. If the return map contains m isolated points, the flow is time–periodic with m minima in the signal of $E(t)$; the time period of the oscillations is estimated by calculating the time difference between $(m + 1)$ consecutive minima. Continuous–looking curves that fill up with points as n increases indicate quasi–periodic behaviour (analogous to flow on a torus), while foldings and geometrical self–similarity provide strong evidence for chaos - see Bergé et al. (1984) for such techniques used in physical experiments; numerical experiments have an advantage over physical experiments in that the data sets can be both much larger and also much more accurate.

ν	Solution type	ν	Solution type	ν	Solution type
0.6	ST	0.034–0.023	TW	0.008	QP
0.574–0.118	TW	0.022–0.018	PTW[1]	0.007	QP
0.117–0.111	PTW[2]	0.017	QP	0.006	QP
0.110–0.096	PTW[1]	0.016–0.014	TW	0.005	QP
0.095–0.046	TW	0.013–0.012	PTW[1]	0.004	QP
0.045–0.037	PTW[1]	0.011	TW	0.003	QP
0.036	PTW[2]	0.01	PTW[56]	0.002	C
0.035	PTW[12]	0.009	QP	0.001	QP

TABLE 1. Dynamical behaviour of the solutions for decreasing values of ν, for $R_e = 25$, $\Lambda = 0.25$, $\Gamma_0 = 1$, $\eta = 1$. Key to solution types: *ST* - stable flow; *TW* - travelling waves; *PTW*[m] - time–periodic travelling waves with m distinct minima in the $E(t)$ signal per time period; *QP* - quasi–periodic oscillations in time; *C* - chaotic oscillations in time.

For parameter values that support travelling wave solutions, the phase speed c is calculated numerically by assuming wave solutions of permanent form given by $H(x,t) = H(x - ct)$, $\Gamma(x,t) = \Gamma(x - ct)$. We can calculate c by computing the solutions at large times; if a travelling wave of permanent form emerges, then c is given by

$$c = \limsup_{t \to \infty} \frac{\int_0^{2\pi} \Gamma_x (H\Gamma)_x \, dx}{\int_0^{2\pi} \Gamma_x^2 \, dx}. \tag{5.11}$$

Once again, the integrals in (5.11) can be calculated with spectral accuracy using Parseval's theorem.

The initial conditions used in all reported simulations (unless stated otherwise) are

$$H(x,0) = \tfrac{1}{10}\nu^{-1/2} \sin x, \qquad \Gamma(x,0) = \Gamma_0 \, \nu^{-1/2}. \tag{5.12}$$

The factor $\nu^{-1/2}$ is used to ensure that for simulations performed for different ν with all other parameters fixed, the undisturbed physical film thickness and base surfactant concentration are the same irrespective of the unscaled domain length $2L$ (recall the transformation (5.1)).

All the results that follow in this section were calculated for initial surfactant concentration $\Gamma_0 = 1$ and surfactant diffusion coefficient $\eta = 1$. The equal viscosity flow having $\Lambda = 0$ was studied first to confirm the results of Bassom et al. (2010). Our main interest lies in identifying the effect of the nonlocal term and the effect of the presence of inertia on the dynamics. To that end, hundreds of numerical experiments were carried out for different values of ν, R_e and $\Lambda \neq 0$. For $R_e = 0$, the flow is found to be stable for $\nu \geqslant 0.516$, in complete agreement with Kalogirou et al. (2012). For $R_e \neq 0$, the flow is unstable if $\Lambda < 0.5$ or $R_e\Lambda^2 > 30$ when the film is more viscous ($\Lambda > 0$), or if $R_e\Lambda^2 < 30$ when the upper fluid is more viscous ($\Lambda < 0$). Numerical solution of the dispersion relation indicates that instability occurs below a critical value ν_c that depends on the values of R_e and Λ.

5.2.1. *Upper (thicker) layer less viscous, $\Lambda > 0$.*

We begin with a typical case $R_e = 25$, $\Lambda = 0.25$, for which the flow is linearly unstable for $\nu < 0.575$. For $\nu \geqslant 0.575$, large–time solutions tend to trivial steady states and non–trivial dynamics arise below this value. The results of extensive large–time computations for different values of ν are displayed in table 1 for the range $0.01 \leqslant \nu \leqslant 0.6$. The different attractors identified in the table are: *TW* - travelling waves of permanent form; *PTW*[m] -
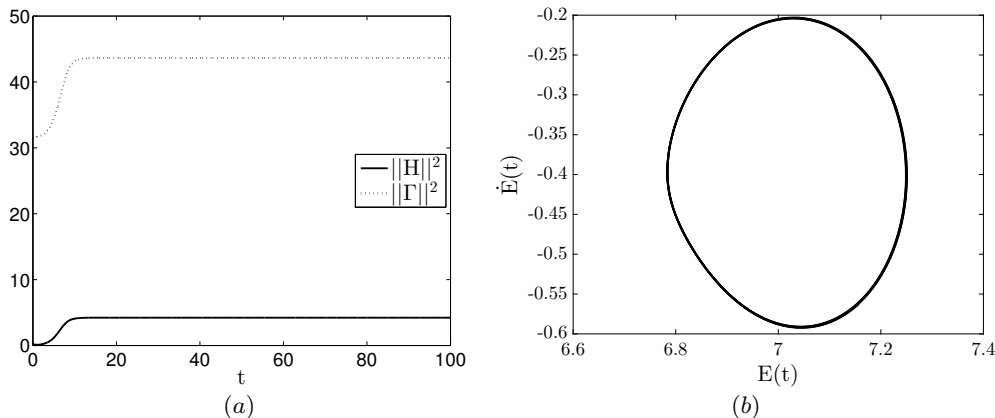
FIGURE 5. Coupled flow for $R_e = 25$, $\Lambda = 0.25$, $\Gamma_0 = 1$, $\eta = 1$. (a) Interfacial (solid) and surfactant (dotted) L_2-norms for $\nu = 0.2$. (b) Phase plane of the energy $E(t)$ for $\nu = 0.1$.

periodic travelling waves that undergo time–periodic oscillations with m distinct minima in the energy signal $E(t)$ (these are waves that after each period of oscillation return to their original form but are shifted spatially by a constant amount); QP - quasi–periodic oscillations in time; C - chaotic oscillations in time.

For values of ν close to (and smaller than) the bifurcation point $\nu_c = 0.575$ and for a relatively broad range of values, the solutions saturate to steady–state travelling waves; oscillations in the energy signal (if they exist) decay and the norms reach constant values. An example of this behaviour is provided in figure 5(a) for $\nu = 0.2$ and it is seen that travelling waves are strongly attracting in the sense that they emerge relatively quickly in time. At $\nu \approx 0.117$ a Hopf bifurcation occurs giving rise to time–periodic travelling waves. As ν decreases from 0.117 to 0.111, the energy $E(t)$ has two minima over its time period. At $\nu \approx 0.11$ another bifurcation occurs with time oscillations supporting one minimum in every period. These bifurcations can be identified by considering the energy phase plane that tends to a closed curve (periodic cycle) after a large time, as shown in figure 5(b) for $\nu = 0.1$. As ν decreases further, travelling wave solutions are interchanged with time–periodic solutions with the pattern persisting until $\nu \approx 0.017$. For $\nu = 0.017$ we find that the large–time solutions converge to a quasi–periodic attractor. To indicate the complexity of the solutions as ν decreases further, we note that for $\nu = 0.01$ the flow is periodic and 56 distinct isolated points can be identified in the return map - the energy $E(t)$ has 56 local minima. As ν becomes even smaller, e.g. $\nu \leqslant 0.009$, the flow gets attracted to complex dynamical behaviour that is mainly quasi–periodic but also chaotic. Figure 6 illustrates return maps and the corresponding energy spectra for $\nu = 0.007$ (panels (a)–(b)) and $\nu = 0.002$ (panels (c)–(d)). The return map for $\nu = 0.007$ consists of a continuous curve topologically equivalent to a circle (cf. flow on a torus) confirming quasi–periodicity, while for $\nu = 0.002$ foldings in the return map are found and these suggest that the flow is chaotic.

Representative plots of the interfacial height H (solid curve) and local surfactant concentration Γ (dashed curve) are provided in figure 7 for all computed windows where travelling waves are found. In the first window which supports travelling waves ($0.118 \leqslant \nu \leqslant 0.574$), the waves are fully modal, i.e. all Fourier modes are present and the spatial period is 2π. Figure 7(a) shows typical solutions from this window for $\nu = 0.2$. In the second travelling wave window ($0.046 \leqslant \nu \leqslant 0.095$) the solutions become bimodal, i.e. their Fourier spectrum contains only even wavenumbers and the spatial period is π, as

(a) *Return map,* $\nu = 0.007$.

(b) *Energy spectra,* $\nu = 0.007$.

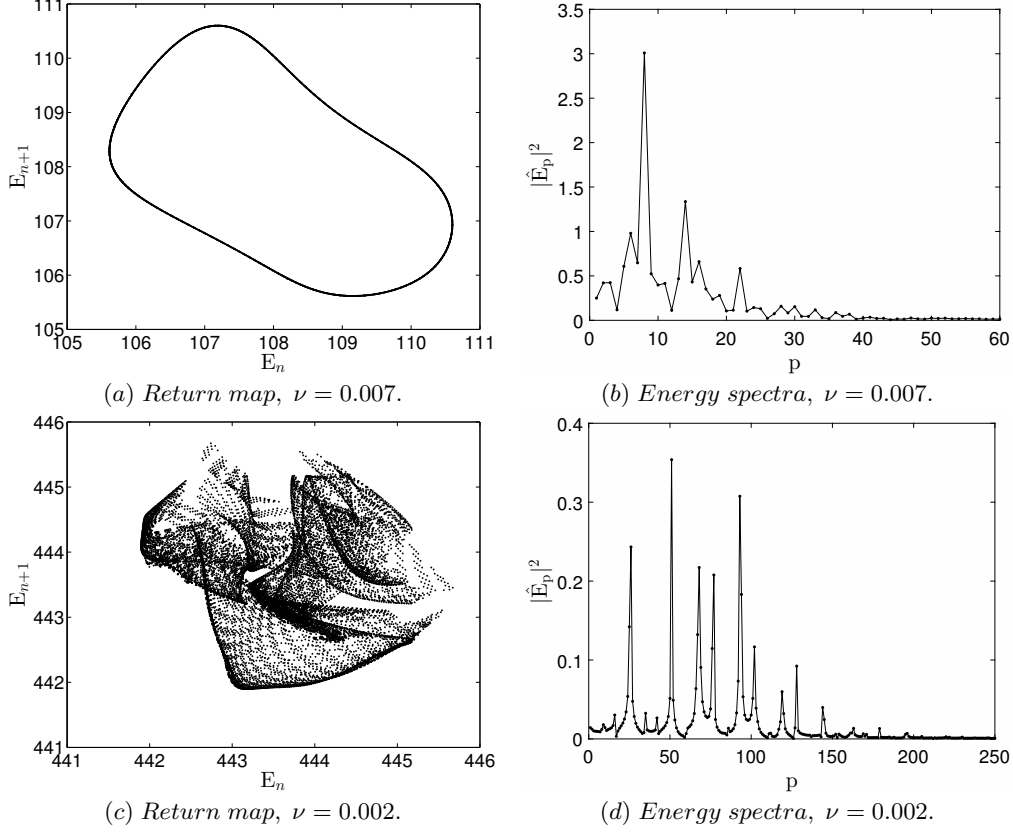(c) *Return map,* $\nu = 0.002$.

(d) *Energy spectra,* $\nu = 0.002$.

FIGURE 6. Return maps and corresponding energy spectra for $\nu = 0.007$ (panels (a) and (b)) and $\nu = 0.002$ (panels (c) and (d)), for $R_e = 25$, $\Lambda = 0.25$, $\Gamma_0 = 1$, $\eta = 1$. In the panels presenting the spectra of the energy signal, $|\hat{E}_p|^2$ denotes the Fourier coefficients found by taking an FFT of the energy signal in time. The results show complex dynamical phenomena, namely quasi–periodicity (results in top row) and chaos (results in bottom row).

illustrated in figure 7(b) for the case of $\nu = 0.09$. As ν decreases further, the travelling wave windows $0.023 \leqslant \nu \leqslant 0.034$, $0.014 \leqslant \nu \leqslant 0.016$ and $\nu = 0.011$ support waves that are tri–, tetra– and penta–modal, respectively, i.e. their basic spatial periods are $2\pi/3$, $\pi/2$ and $2\pi/5$ and their non–zero Fourier modes are multiples of 3, 4 and 5, respectively. Figures 7(c)–7(e) illustrate such solutions for $\nu = 0.03$, $\nu = 0.015$ and $\nu = 0.011$. The results of figure 7 also show that as ν is reduced the amplitudes of the interfacial waves as well as the surfactant concentration increase. In fact their increase is proportional to $\nu^{-1/2}$ as found in our computations (Kalogirou 2014), confirming that the unscaled amplitudes remain of order one as seen from the transformation (5.1).

Another notable feature of the solutions presented in figure 7 is that the surfactant concentration attains a local maximum or minimum in the vicinity of points where $H = 0$ (this feature also appears in figure 10 presented later). To explain this physically we consider the total velocity at the interface $u_I = \overline{U}_I(\epsilon) + m\epsilon^2 H + \epsilon^3 U_1 + \mathcal{O}(\epsilon^4)$, which shows that the leading order perturbation of order $\mathcal{O}(\epsilon^2)$ is equal to mH. This in turn implies that in the frame of reference moving with the undisturbed interfacial velocity, the horizontal velocity changes sign at points x^* where $H(x^*) = 0$ - the point x^* is a local stagnation point, to leading order and in the moving frame. The flow is inwards towards x^* if $H'(x^*) < 0$ and outwards if $H'(x^*) > 0$; in the former case the inwards
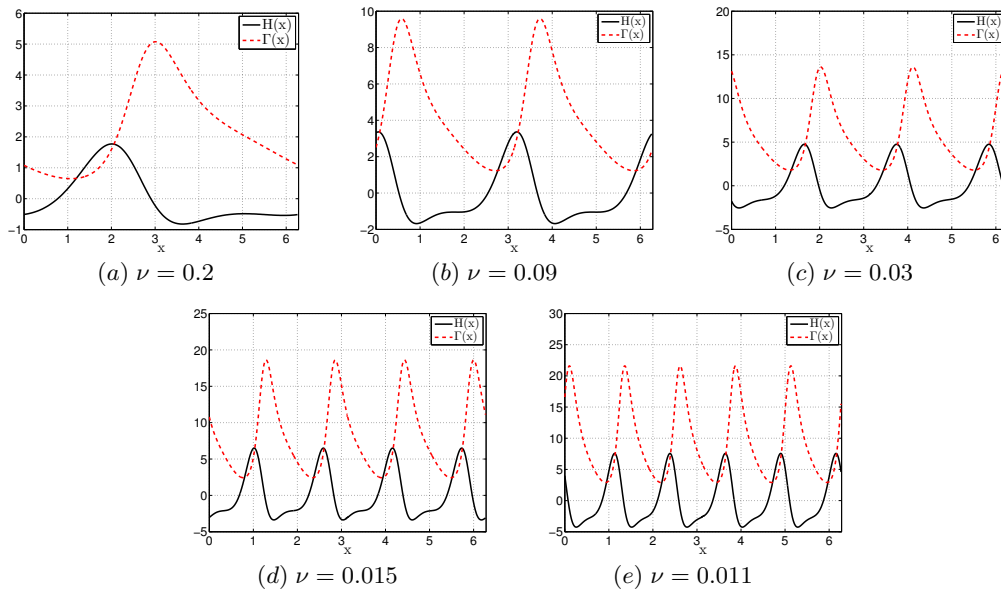
FIGURE 7. Wave profiles $H(x)$ (solid) and $\Gamma(x)$ (dashed) at time t=100, for $R_e = 25$, $\Lambda = 0.25$, $\Gamma_0 = 1$, $\eta = 1$. Each panel corresponds to a $n-$modal travelling wave with spatial period $2\pi/n$, $n = 1, \ldots, 5$, respectively.

flow sweeps surfactant to the vicinity of x^* and so provides a local increase in surfactant concentration leading to a maximum in Γ there - see figure 10 for regions ahead of local maxima of H. When $H'(x^*) > 0$ the flow sweeps surfactant away from x^* and hence leads to a local minimum in Γ (i.e. a depletion of surfactant) just behind local maxima of H. Similar findings were reported in a study of surfactant–laden core–annular flows by Kas-Danouche et al. (2009).

5.2.2. *Upper (thicker) layer more viscous, $\Lambda < 0$.*

We begin by presenting solutions for $\Lambda = -0.25$, for which the flow is unstable for Reynolds numbers $R_e < 480$ - we fix $R_e = 25$. For these parameters the flow is linearly unstable for $\nu < 0.55$ and the solutions are mostly travelling waves of permanent form, except for $0.049 \leqslant \nu \leqslant 0.053$ where the solutions are time–periodic travelling waves. Numerical calculations were performed for ν as small as 0.01, but no intricate structures were observed (i.e. quasi–periodicity or chaos). In figure 8(a) the variation of the wave speed c with ν is shown for all computed windows where travelling waves of permanent form emerge, while figure 8(b) depicts the variation of the period of oscillation with ν for solutions in the time–periodic window. It is seen that the travelling wave speed is monotonically decreasing as ν deceases, while in the case of time–periodic travelling waves the period of oscillation increases monotonically as ν decreases. The breaks in the curves of figure 8(a) are due to the existence of different solution branches at the same parameter values (this is caused by the nonlinearity - see Kevrekidis et al. (1990) for a detailed bifurcation study of the various solutions of the Kuramoto–Sivashinsky equation).

Next we consider the effect of the Reynolds number on the characteristics of the flow for fixed ν (i.e. fixed domain size). We took the representative value $\nu = 0.1$ and performed numerical calculations for the range of Reynolds numbers $0 \leqslant R_e \leqslant 100$. We find that solutions develop into travelling waves for the ranges $0 \leqslant R_e \leqslant 4$ and $31 \leqslant R_e \leqslant 100$;
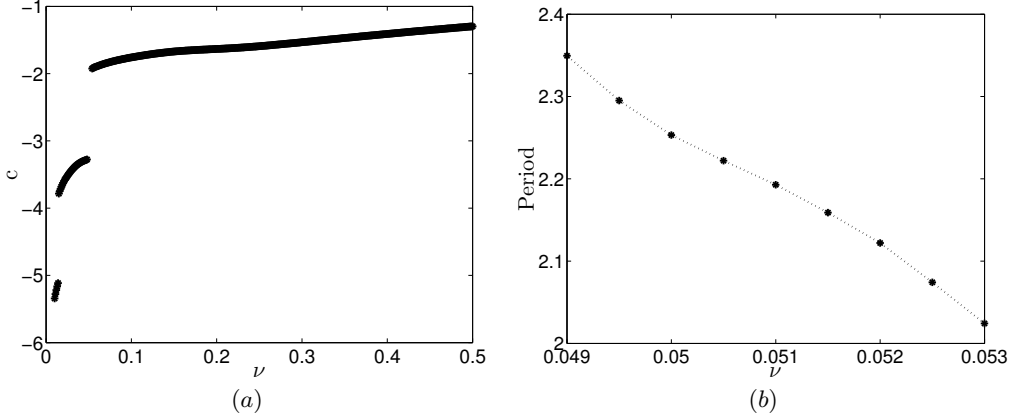
FIGURE 8. Characteristics of (a) travelling wave speeds, and (b) periods of oscillation for time–periodic travelling waves, for $R_e = 25$, $\Lambda = -0.25$, $\Gamma_0 = 1$, $\eta = 1$.
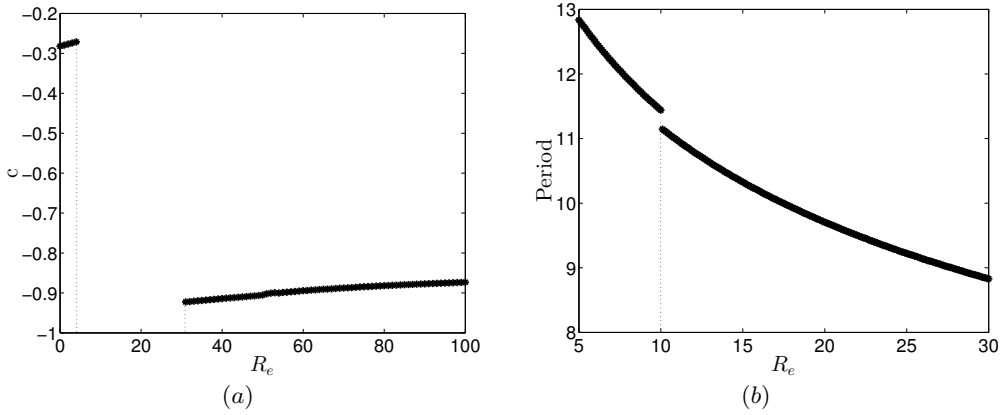

FIGURE 9. Effect of the Reynolds number R_e on (a) travelling wave speeds, and (b) periods of oscillation for time–periodic travelling waves, for $\nu = 0.1$, $\Lambda = 0.25$, $\Gamma_0 = 1$, $\eta = 1$.

the variation of the travelling wave speed c with R_e is shown in figure 9(a). As can be seen from the figure, no travelling waves emerge for the range $5 \leqslant R_e \leqslant 30$; the solutions here are time–periodic travelling waves instead and their period of oscillation is depicted in figure 9(b). The travelling waves on either side of the time–periodic window belong to different bifurcation branches as confirmed by inspection of figure 9(a). Interestingly, the time–periodic travelling wave window is also split into two distinct branches above and below $R_e \approx 10$. Our initial value problem computations converge to the most attracting solutions, and we have confirmed this numerically by starting with different initial conditions from (5.12) (namely $H(x,0) = \frac{1}{10}\nu^{-1/2}(\sin x + 0.5\cos 2x)$, $\Gamma(x,0) = \Gamma_0\,\nu^{-1/2}$), in which case we obtain different travelling wave solutions at the same parameters - a numerical bifurcation study can fully map out such structures but this is not pursued further here. An overall physical feature of the results is that the wave speed c is negative and increases with the Reynolds number, at least where stable travelling waves exist. Furthermore, the period of oscillation of time–periodic travelling waves (where they are supported) is found to decrease monotonically with the Reynolds number.

We conclude this section by presenting solution features from different regions of the stability diagram 2. To fix matters we take $\Gamma_0 = 1$, $\eta = 1$ which in turn provide the
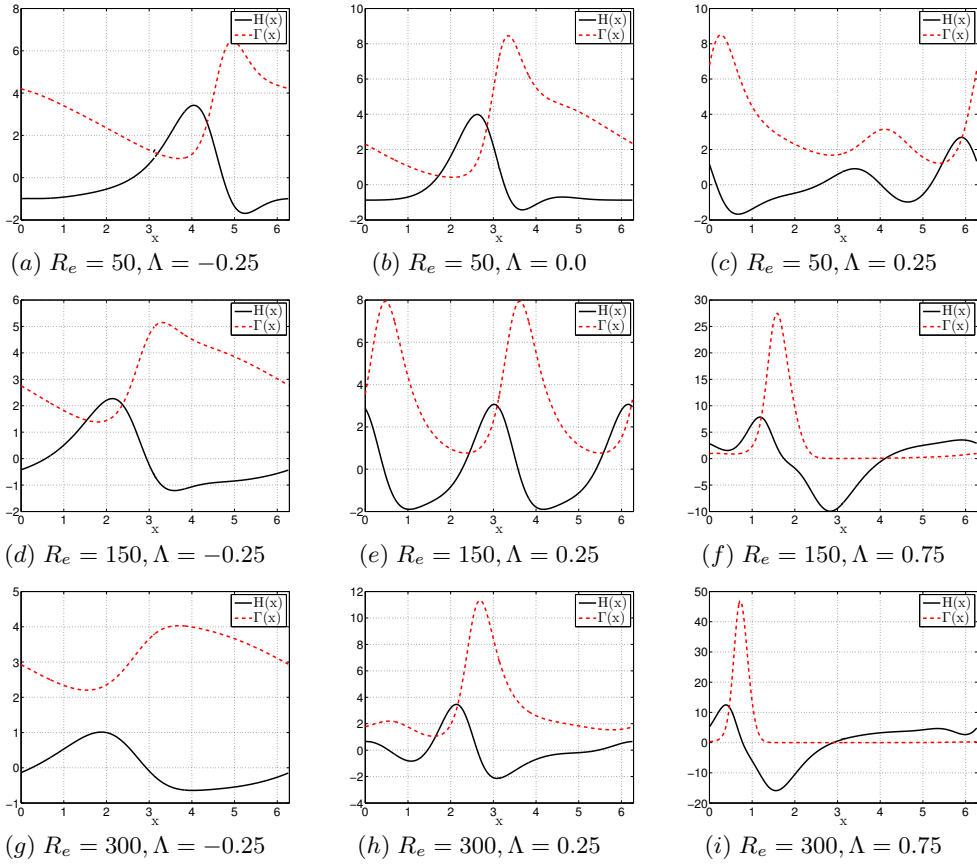
FIGURE 10. Representative wave profiles $H(x)$ (solid) and $\Gamma(x)$ (dashed) for different values of Λ and $R_e = 50$ (top row), $R_e = 150$ (middle row), $R_e = 300$ (bottom row) and $\nu = 0.1$, $\Gamma_0 = 1$, $\eta = 1$.

critical values $\Lambda_c = 0.5$ and $R_{ec} = 120$ (recall from figure 2 that the flow can be linearly stable if $\Lambda > \Lambda_c$ and $R_e < R_{ec}$, or if $\Lambda < 0$ and $R_e > R_{ec}$). To quantify the effect of the Reynolds number and viscosity ratio on the flow, we computed the large–time solutions for a range of R_e and Λ. Here, we consider three different Reynolds numbers $R_e = 50, 150, 300$ and for each one we compute the large–time behaviour of the solutions for three values of Λ from the linearly unstable region (the shaded area) in figure 2. The computed solutions are travelling waves in all nine cases and are depicted in figure 10. The top row corresponds to $R_e = 50 < R_{ec} = 120$ and $\Lambda = -0.25$ (left panel), $\Lambda = 0$ (middle panel), $\Lambda = 0.25 < \Lambda_c = 0.5$ (right panel), with each panel showing the interfacial profile (solid curve) and the corresponding local surfactant concentration (dashed curve). The amplitude of the interfacial profile increases when Λ varies from -0.25 to 0, but then decreases again when Λ changes to 0.25. In fact it is found that as Λ gets closer to the critical value $\Lambda_c = 0.5$, the solution amplitudes decrease to zero. Such non-monotonic behaviour has also been computed in the case $R_e = 0$ (see Kalogirou et al. (2012) and the bifurcation diagram in their figure 3b). An additional feature when inertia is present, is that a sufficiently large Λ produces a non–trivial travelling wave solution as expected from the stability diagram in figure 2 (we have confirmed that a travelling wave emerges when $\Lambda = 0.8$ - another branch of bifurcating travelling waves

will start at $\Lambda \approx \sqrt{3/5}$). At the value $R_e = 150$ which is above the critical R_{ec}, an increase in Λ to positive values does not suppress the instability as in the previous case that supports a stability window; results are shown in the middle row for the values $\Lambda = -0.25$ (left), $\Lambda = 0.25$ (middle) and $\Lambda = 0.75$ (right). These results indicate that the wave amplitudes increase with Λ - in fact the interfacial amplitudes are approximately equal to 3, 5 and 17 for Λ equal to -0.25, 0.25 and 0.75, respectively. The final row in figure 10 corresponds to $R_e = 300$ with $\Lambda = -0.25$ (left), $\Lambda = 0.25$ (middle) and $\Lambda = 0.75$ (right); once again we can conclude that the solution amplitudes increase as Λ increases, analogously to the case of a lower R_e. Another observation supported by our results is that for a fixed $\Lambda < 0$, the amplitudes of the solutions decrease as R_e increases since in this case the Reynolds number has a stabilising effect on the flow - for example, see the results for $\Lambda = -0.25$ in the first column of figure 10. On the other hand, if $\Lambda > 0$ and fixed, increasing the Reynolds number leads to an increase in the solution amplitudes (see the panels corresponding to $\Lambda = 0.25$ in figure 10); such behaviour is consistent with the linear stability results summarised in figure 2.

6. Emergence of three–dimensional flows due to secondary spanwise instabilities

In the numerical results presented above we have shown that nonlinear travelling waves can be found for different values of the parameters ν, R_e and Λ. Physically, the system may also be susceptible to spanwise perturbations, and it is important to establish whether computed one–dimensional interfacial coherent structures are stable. In what follows we consider the stability (to spanwise perturbations) of travelling waves of the form $\overline{H}(\xi)$ and $\overline{\Gamma}(\xi)$, where $\xi = x - ct$ and c is the speed of propagation. Note that such waves are stable to streamwise disturbances in the $x-$direction (of wavelengths no longer than the computational period) since they are computed as large–time solutions of initial value problems. One–dimensional interfacial travelling waves are characterised by a constant energy at large times and analogous diagnostics are used for three–dimensional flows by defining the energy

$$||H(\cdot, \cdot, t)||_2^2 = \int_0^{2\pi} \int_0^{2\pi} H^2(x, z, t) \, \mathrm{d}x \, \mathrm{d}z. \tag{6.1}$$

We first investigate the linear stability of one–dimensional interfacial travelling wave solutions to three–dimensional disturbances by writing

$$H(\xi, z, t) = \overline{H}(\xi) + \tilde{H}(\xi, z, t), \quad \Gamma(\xi, z, t) = \overline{\Gamma}(\xi) + \tilde{\Gamma}(\xi, z, t). \tag{6.2}$$

Linearising with respect to tilde quantities and looking for solutions in the form

$$\tilde{H} = f(\xi) \, \mathrm{e}^{\lambda t} \, \mathrm{e}^{ik_2 z}, \qquad \tilde{\Gamma} = g(\xi) \, \mathrm{e}^{\lambda t} \, \mathrm{e}^{ik_2 z}, \tag{6.3}$$

where $f(\xi)$ and $g(\xi)$ are $2\pi-$periodic, yields the following coupled system of ODEs to determine the eigenvalue λ,

$$\lambda f + \left(\overline{H} f\right)_\xi + \nu_1 \left(\partial_\xi^2 - \frac{\nu_2}{\nu_1} k_2^2\right)^2 f + \widehat{\mathcal{P}}_{k_2} f - \left(\partial_\xi^2 - \frac{\nu_2}{\nu_1} k_2^2\right) g = 0, \tag{6.4a}$$

$$\lambda g + \left(\overline{H} g\right)_\xi + \left(\overline{\Gamma} f\right)_\xi - \eta \left(\partial_\xi^2 - \frac{\nu_2}{\nu_1} k_2^2\right) g = 0. \tag{6.4b}$$

The term $\widehat{\mathcal{P}}_{k_2}$ is the Fourier transform of the pseudo–differential operator $\mathcal{P}$ with respect to z. The system is next cast into a matrix problem that can be readily used to compute
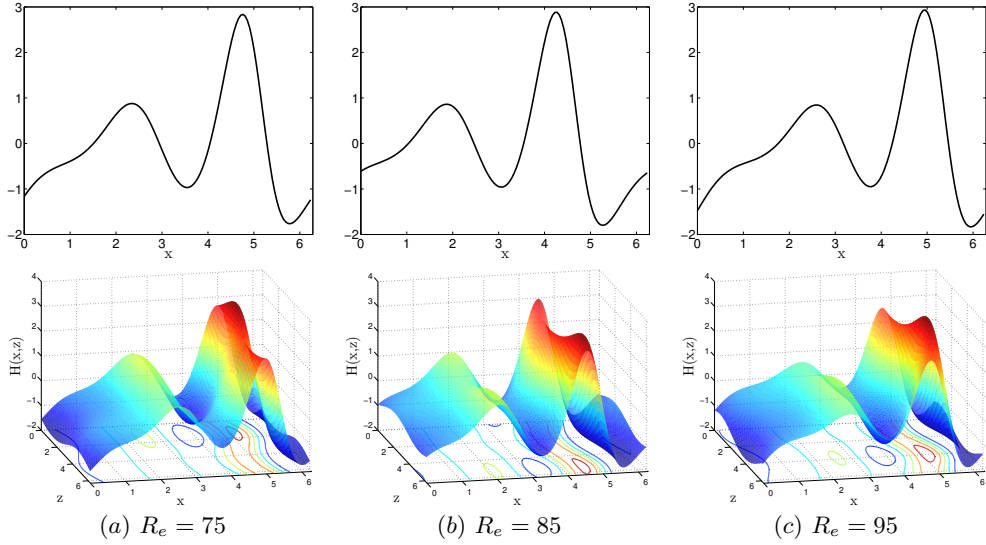
FIGURE 11. Interfacial profiles for $\nu = 0.1$, $\Lambda = 0.25$, $\Gamma_0 = 1$, $\eta = 1$ and $R_e = 75$ (left column), $R_e = 85$ (middle column), $R_e = 95$ (right column). The profiles in the top row are obtained from the one–dimensional initial value problem with the initial conditions (5.12). The bottom row depicts fully two–dimensional interfacial solutions for $\nu_1 = \nu_2 = 0.1$.

the eigenvalues, by representing $f(\xi)$ and $g(\xi)$ in terms of their Fourier coefficients (this is also done for $\overline{H}(\xi)$ and $\overline{\Gamma}(\xi)$ which have known Fourier coefficients). The Fourier series are truncated appropriately to provide a finite–dimensional eigenvalue problem for $\lambda(k_2; \nu_1, \nu_2, R_e, \Lambda, \Gamma_0, \eta)$, which is then solved for integer values of k_2 (for every value of $k_2 \in \mathbb{Z}_+$, a stability curve similar to figure 3 is obtained). If the real part of λ is positive for any k_2, then instability is supported for spanwise perturbations of wavelength $2\pi/k_2$ (note that due to translational invariance in the $x-$direction, $\lambda = 0$ is always an eigenvalue). In practice, since the system is long–wave unstable, setting $k_2 = 1$ and looking for at least one λ with positive real part is a sufficient condition for spanwise instability.

The analysis described above was first used to study the stability of the nonlinear one–dimensional interfacial travelling wave solution branches given in figure 9(a). The spectra were computed to establish (results not given for brevity) that both branches are linearly unstable to spanwise disturbances. Rather than presenting eigenvalue plots, we have followed the instabilities into the nonlinear regime to compute the two–dimensional solutions that arise. We solve the PDEs (5.5)–(5.6) subject to initial conditions

$$H(x, z, 0) = \overline{H}(\xi) + \mathcal{R}(z), \qquad \Gamma(x, z, 0) = \overline{\Gamma}(\xi) + \mathcal{R}(z), \tag{6.5}$$

where

$$\mathcal{R}(z) = \sum_{m=1}^{N} \left(\alpha_m \sin mz + \beta_m \cos mz \right), \tag{6.6}$$

and $\alpha_m, \beta_m \in [-0.1, 0.1]$ are random Fourier coefficients; in the runs presented here we also pick $N = 5$ - larger wavenumbers are damped significantly so this choice is appropriate. Typical results were computed for $\nu_1 = \nu_2 = 0.1$ and $R_e = 75, 85, 95$ (other parameters are as in figure 9(a)), and the results are shown in figure 11. The panels in the top row show the unstable one–dimensional interfacial travelling waves $\overline{H}(\xi)$, while the panels in the bottom row provide the stable two–dimensional interfacial travelling waves at the three different values of R_e.
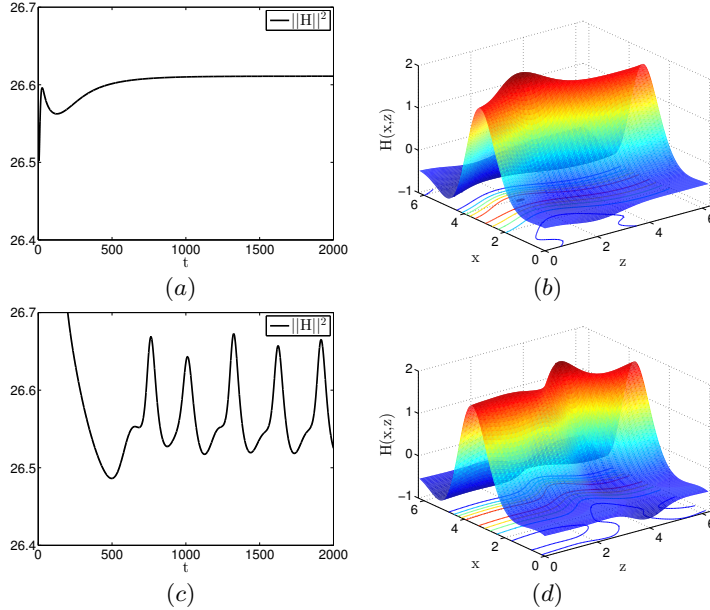
FIGURE 12. Energy of two–dimensional solutions (left column) and interfacial profiles (right column) for $Re = 25$, $\Lambda = 0.25$, $\Gamma_0 = 1$, $\eta = 1$. (a)+(b) $\nu_1 = 0.2$, $\nu_2 = 0.03$: interfacial travelling wave. (c)+(d) $\nu_1 = 0.2$, $\nu_2 = 0.0085$: time–periodic interfacial travelling wave. Both profiles are taken at time $t = 2000$.

We also found that the flow can be linearly unstable to spanwise perturbations for several other choices of the parameter values. We illustrate the underlying instabilities by presenting numerical solutions of the nonlinear evolution equations (5.5)–(5.6) for the three set of parameter values corresponding to the marked points in figure 2. The first set of results are for $Re = 25$, $\Lambda = 0.25$, $\Gamma_0 = 1$, $\eta = 1$. These parameters correspond to the point 'o' in the stability diagram in figure 2 - here the flat uniform state is unstable to streamwise perturbations and nonlinear travelling waves $\overline{H}(\xi)$ and $\overline{\Gamma}(\xi)$ arise. These travelling waves are computed by solving the one–dimensional equations (5.7)–(5.8) with $\nu = 0.2$, in order to find $\overline{H}(\xi)$ and $\overline{\Gamma}(\xi)$ to be used in (6.5) (more precisely, the travelling waves are recorded at $t = 2000$, long after any transient dynamics). Perturbations in the $z-$direction are added according to (6.5)–(6.6) and new initial value problems are solved by fixing $\nu_1 = 0.2$ and taking decreasing values of ν_2 starting from $\nu_2 = 0.2$, i.e. starting from a wave on a square domain, and allowing the unscaled spanwise period to increase as ν_2 decreases. We find that until approximately $\nu_2 = 0.06$, the nonlinear solution is stable to spanwise disturbances and remains independent of z. As ν_2 decreases below 0.06, spanwise modes become unstable and two–dimensional interfacial travelling wave solutions emerge in the direction of the underlying flow. An example of such a solution is given for $\nu_2 = 0.03$ (in unscaled terms the wave dimensions are approximately 14×36 units) in figures 12(a) and (b), that show the evolution of the energy (6.1) and the interfacial profile H at $t = 2000$, respectively. As ν_2 is decreased further a Hopf bifurcation takes place that leads to time–periodic travelling waves as can be seen by the case $\nu_2 = 0.0085$ (an unscaled domain of dimensions 14×68, approximately), shown in figures 12(c)–(d). The time–periodicity can be seen from the energy signal in panel (c) and the three–dimensionality of the flow is clearly identified by the interfacial profile in panel (d), selected at $t = 2000$.

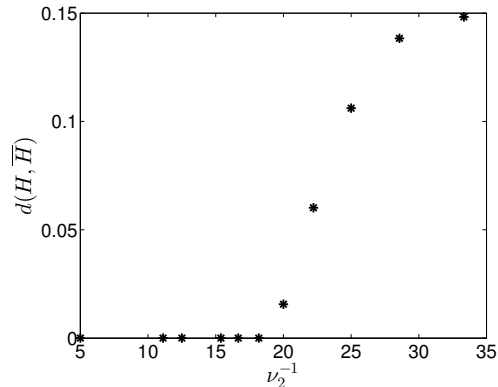The three–dimensionality of the flow was also quantified by calculating the difference

FIGURE 13. Measure of three–dimensionality defined in (6.7) for $\nu_1 = 0.2$ and $Re = 25$, $\Lambda = 0.25$, $\Gamma_0 = 1$, $\eta = 1$.

of the L_2-norms of the travelling wave profiles supported for every ν_2,

$$d(H, \overline{H}) = ||H(x, z, t)||^2 - ||\overline{H}(\xi)||^2. \tag{6.7}$$

The results are shown in figure 13 as a function of ν_2^{-1} for those values of ν_2 which support travelling wave solutions. For $0.06 \leqslant \nu_2 \leqslant 0.2$ the measure $d(H, \overline{H}) = 0$, confirming that the travelling waves remain one–dimensional. For $\nu_2 < 0.06$, two–dimensional interfacial waves emerge and become more pronounced as ν_2 decreases. This pattern continues until $\nu_2 \approx 0.03$, below which a Hopf bifurcation takes place as discussed earlier.

When $\Lambda < 0$, i.e. the less viscous liquid is in the thin layer, the base–state in the absence of surfactants is linearly stable to two–dimensional perturbations but can be unstable in their presence. Such a case is noted on figure 2 with a star symbol for the parameters $Re = 25$, $\Lambda = -0.25$, $\Gamma_0 = 1$, $\eta = 1$ and a computation of the evolution equations (5.7)–(5.8) with $\nu = 0.25$ produces nonlinear one–dimensional interfacial travelling waves as expected. Even though the base–state is stable to three–dimensional perturbations on a square domain at these parameter values, the one–dimensional interfacial travelling waves can lose stability to sufficiently long spanwise perturbations (equivalently if ν_2 is sufficiently small in our scaled system (5.5)–(5.6)). The emerging solutions are travelling waves in the direction of the flow with two–dimensional interfacial and surfactant distributions. These results are illustrated in figure 14 for the parameters given above; panel (a) on the left depicts the one–dimensional travelling wave interface (extended in the spanwise direction for illustration purposes), while panel (b) shows the large–time solution that results by perturbing this for $\nu_2 = 0.01$. Both solutions are taken at $t = 2000$ units which is sufficiently large for transients to die out. The three–dimensionality is clearly discernible and the profiles are qualitatively similar to those for $\Lambda = 0.25$ given in figure 12.

Finally, we consider cases for which the base flow is stable to two–dimensional linear perturbations but unstable to three–dimensional ones. As discussed already in §4.2, in the presence of surfactants Squire's theorem does not hold for order one Reynolds numbers and we wish to follow such three–dimensional instabilities into the nonlinear regime. The example we select has parameters $Re = 35$, $\Lambda = -1.0$, $\Gamma_0 = 1$, and $\eta = 1$ - this is represented by a symbol 'x' in the two–dimensional stability diagram in figure 2 and is seen to be in the stable region. One–dimensional interfacial travelling wave solutions do not emerge in this case (at least for all initial conditions tested here - this is expected if the initial conditions are not too large) and computations are carried out by perturbing
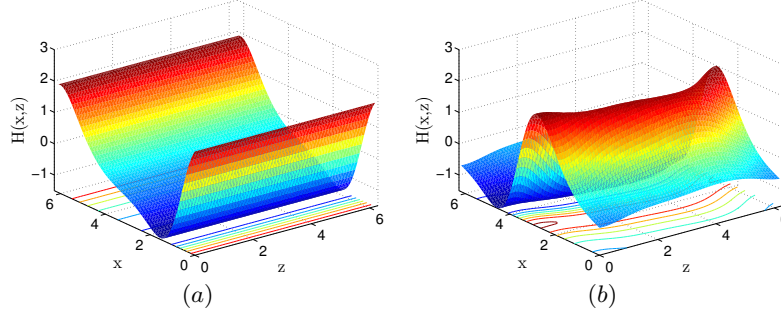
FIGURE 14. Interfacial wave profiles for $Re = 25$, $\Lambda = -0.25$, $\Gamma_0 = 1$, $\eta = 1$. (a) $\nu = 0.25$: one–dimensional travelling wave due to surfactant–induced instability. (b) $\nu_1 = 0.25$, $\nu_2 = 0.01$: three–dimensional flow with a two–dimensional interfacial travelling wave profile. All profiles are taken at time $t = 2000$ and travel along the x–axis.

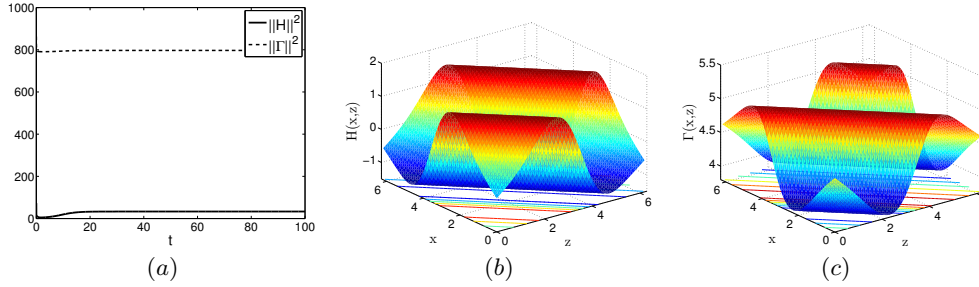

FIGURE 15. L_2–norms and profiles showing interfacial shape and surfactant concentration at $t = 100$. The parameter values used are $\nu_1 = \nu_2 = 0.05$ and $Re = 35$, $\Lambda = -1.0$, $\Gamma_0 = 1$, $\eta = 1$. The corresponding two–dimensional flow is stable.

the flat base state. A representative example is given in figure 15 for $\nu_1 = \nu_2 = 0.05$ (a square domain of size 28×28, approximately). Panel (a) shows the evolution of the energy norms of the interface and the surfactant concentration ($\|H\|^2$ and $\|\Gamma\|^2$, respectively), while panels (b) and (c) show the corresponding profiles at $t = 100$, after the transient phase. The waves travel at an angle of $45°$ relative to the basic flow and are seen to be one–dimensional in the rotated frame, i.e. they are functions of $x + z - ct$ where c is the speed of propagation. The emergence of these non–trivial waves for a set of parameter values that produce trivial solutions in two–dimensional flows can be explained by the shift of the stability curve in figure 2, producing a larger region of instability for $\Lambda < 0$ (see the discussion in §4) so that the point marked 'x' now falls into the unstable (grey) region.

It should be stressed that all of the two–dimensional interfacial solutions presented above are stable to perturbations that are no longer than the basic period in either the streamwise or spanwise direction. It would be interesting to consider longer wave perturbations to establish if the solutions are also modulationally stable, something that has not been addressed for multidimensional Kuramoto–Sivashinsky type equations (for the one–dimensional KS equation the reader is referred to Barker et al. (2013), Frisch et al. (1986), Papageorgiou et al. (1992)). This is left for future investigations.

7. Conclusions

In this paper, the problem of two–layer Couette flows in the presence of surfactants is tackled analytically and numerically. Asymptotic analysis is used to derive a set of evo-

lution equations for the interfacial shape and the local surfactant concentration on the interface. The analysis assumes that one of the layers is thin and that weakly nonlinear waves form with wavelengths that scale with the channel thickness. An interaction between the thin and thick layers produces a nonlocal coupling into the interfacial dynamics; the coupling arises by solving an Orr–Sommerfeld type problem in the thick layer that is valid at arbitrary (but not asymptotically large) Reynolds numbers. Two– and three–dimensional flows are considered and evolution equations are derived in both cases. The dynamical behaviour of the system is explored by undertaking extensive computations for a wide range of parameter values.

The nonlocal models derived here retain all salient physical mechanisms associated with two–fluid shear flows as we briefly list next. These include the inertial long–wave destabilisation of two–layer Couette (or Couette–Poiseuille) flows at non–zero Reynolds numbers (Yih 1967) - this instability exists if the thinner fluid layer is more viscous, otherwise the flow is stable at any Reynolds number (Hooper 1985). Addition of surfactant can destabilise the flow even in the absence of inertia and independent from viscosity ratio values (even for equal viscosity fluids), see Frenkel & Halpern (2002); Halpern & Frenkel (2003). Moreover, inertial effects increase the growth of the surfactant–induced Marangoni instability and therefore produce new regions of instability as noted by Pozrikidis (2004); Blyth & Pozrikidis (2004a); Frenkel & Halpern (2005). All of these physical mechanisms and their linear stability ramifications are summarised in the typical stability diagram in figure 2. The main objective of this work is to follow underlying instabilities into the nonlinear regime using our model and to obtain a complete picture of the dynamics that can arise.

The controlling parameters in our model equations are the Reynolds number R_e, the parameter Λ that involves the scaled Capillary number and the viscosity ratio (see (3.12) - this parameter can be positive or negative depending on the viscosity ratio), a dimensionless surfactant diffusion coefficient η, as well as the size(s) of the periodic domain where the computations are carried out. The latter are crucial in studying the dynamical complexity of such long–wave unstable systems; as the domain size increases, additional linearly unstable modes enter and affect the nonlinear solutions.

Extensive computations are carried out for $\Lambda > 0$ (upper layer less viscous - linearly unstable in the absence of surfactants) and $\Lambda < 0$ (upper layer more viscous - linearly stable in the absence of surfactants). For $\Lambda > 0$ and in the case of two–dimensional flows at finite R_e, our computations reveal that as the system size increases (equivalently the parameter ν decreases) solutions get attracted to steady–state travelling waves, time–periodic travelling waves, as well as quasi–periodic oscillations and spatiotemporal chaos (see table 1 for details in the case $\Lambda = 0.25$, $R_e = 25$, $\Gamma_0 = 1$, $\eta = 1$). One notable difference between the present results and the inertialess ones of Kalogirou et al. (2012), is that chaos is supported on much smaller domains when $R_e \neq 0$. For example, when $R_e = 0$ a domain size of at least 100 units is required to see spatiotemporal chaos, whereas for $R_e = 25$ it occurs for domains of approximately 30 units - see table 1. As the Reynolds number increases, therefore, chaotic solutions can emerge in relatively shorter channels.

When $\Lambda < 0$ instabilities set in due to Marangoni effects. Computations into the nonlinear regime reveal that the dynamical complexity found for $\Lambda > 0$ is no longer supported. Once again the most prevalent states are nonlinear travelling waves that undergo Hopf bifurcations to produce time–periodic travelling waves for a wide range of parameters. A particular feature is that the speed of the waves increases with the length of the domain (see figure 8, for example, for $R_e = 25$ and $\Lambda = -0.25$) in regions where travelling waves are supported. In addition, the speed of travelling waves is found to increase weakly with

R_e, and in regions where time–periodic solutions exist their period decreases with R_e (see figure 9 for an example). It is also found that for a given $\Lambda < 0$, sufficiently large Reynolds numbers stabilise the flow. An inertial stabilisation of the Marangoni instability is developed as can be anticipated from figure 2 and confirmed through nonlinear computations. In addition, if Λ is sufficiently large and negative, solutions are found to tend to the trivial flat state for fairly arbitrary initial conditions and any R_e (again observed in figure 2). This is due to a stabilisation of the Marangoni instability by a competing (stabilising) viscosity stratification.

The present study also investigated the dynamics of three–dimensional flows and the stability of nonlinear one–dimensional interfacial travelling waves. At zero Reynolds number, a Squire's type theorem holds and so two–dimensional perturbations are the most unstable. We have shown that this is no longer the case when inertia is present - see for example the symbol 'x' in figure 2, where two–dimensional perturbations are linearly stable but three–dimensional ones are not. It is also established that under certain conditions, wave shapes that are one–dimensional interfacial travelling waves can lose stability to spanwise perturbations to produce three–dimensional flows and novel two–dimensional interfacial waves that travel in the direction of the underlying shear. Such secondary instabilities are found when inertia is present ($R_e \neq 0$) and for both less and more viscous films (see for example figures 11, 12 and 14).

A. **Asymptotic properties of** $\mathcal{N}(k_1, k_2)$

We begin by considering small values of k_1 and k_2 (i.e. the long–wave limit) in order to localise the pseudo–differential operator (see Smyrlis & Papageorgiou (1998) for comparisons between solutions of local and nonlocal PDEs of the Kuramoto–Sivashinsky type). To achieve this we consider a Taylor expansion of $F(y)$ in powers of k_1, k_2 in equation (3.7a), resulting in the leading order expression

$$F''(0) = -4 - \frac{iR_e}{30}k_1 - \left(\frac{4}{15} + \frac{R_e^2}{4200}\right)k_1^2 - \frac{4}{15}k_2^2 + \cdots, \qquad (A\,1)$$

and thus

$$\mathcal{N}(k_1, k_2) \approx 2k_1 + \frac{iR_e}{60}k_1^2 + \left(\frac{2}{15} + \frac{R_e^2}{8400}\right)k_1^3 + \frac{2}{15}k_1k_2^2, \qquad (A\,2)$$

correct to second–order terms inclusive.

The short–wave asymptotic expression of $\mathcal{N}(k_1, k_2)$ as $k_{1,2} \to \infty$, can be also obtained in an analogous manner. In this case the asymptotic solution for $F(y)$ can be found using boundary layer theory (near $y = 0$) and the method of matched asymptotic expansions. The leading order asymptotic form of $\mathcal{N}(k_1, k_2)$ as $k_{1,2} \to \infty$ is found to be

$$\mathcal{N}(k_1, k_2) \sim k_1 k + \frac{iR_e}{4}\frac{k_1^2}{k^2}, \quad k_1, \, k_2 \gg 1, \qquad (A\,3)$$

where $k = \sqrt{k_1^2 + k_2^2}$. For details the reader is referred to Kalogirou (2014).

B. **Numerical time–stepping scheme**

In what follows we present and analyse the schemes for the one–dimensional system (5.7)–(5.8), noting that the two–dimensional system (5.5)–(5.6) is treated analogously (see also Kalogirou (2014); Kalogirou et al. (2015)).

Following Akrivis et al. (2011a), we write (5.7)–(5.8) as

$$\boldsymbol{u}_t + \boldsymbol{\mathcal{L}}\boldsymbol{u} = \boldsymbol{\mathcal{B}}(\boldsymbol{u}), \tag{B 1}$$

where $\boldsymbol{u} = (u_1, u_2)^T = (H, \Gamma)^T$ and

$$\boldsymbol{\mathcal{L}} = \begin{pmatrix} \frac{c}{\nu} + \nu\partial_x^4 + \mathcal{P} & 0 \\ 0 & -\eta\partial_x^2 + \eta \end{pmatrix}, \quad \boldsymbol{\mathcal{B}}(\boldsymbol{u}) = \begin{pmatrix} -u_1\partial_x u_1 + \frac{c}{\nu}u_1 + \partial_x^2 u_2 \\ -\partial_x(u_1 u_2) + \eta u_2 \end{pmatrix}, \quad \text{(B 2)}$$

where the constant $c > 0$ is determined later. The form (B 1) fits the class of abstract equations analysed by Akrivis & Crouzeix (2004); they showed that if (i) the symmetric part of $\boldsymbol{\mathcal{L}}$ is self–adjoint and positive–definite, and (ii) $\boldsymbol{\mathcal{B}}$ is locally Lipschitz continuous, then linearly implicit methods are proved to converge to solutions of the PDEs. The constant c is selected in order to ensure self–adjointness as we discuss briefly next - see also (Akrivis et al. 1998, 2011a,b; Akrivis & Smyrlis 2004, 2010).

We begin by writing $\boldsymbol{\mathcal{L}} = \boldsymbol{\mathcal{A}} + \boldsymbol{\mathcal{D}}$ where $\boldsymbol{\mathcal{A}}$ is the symmetric part and $\boldsymbol{\mathcal{D}}$ the antisymmetric part (i.e. $\boldsymbol{\mathcal{D}}$ is a dispersive operator),

$$\boldsymbol{\mathcal{A}} = \begin{pmatrix} \mathcal{A}_1 & 0 \\ 0 & \mathcal{A}_2 \end{pmatrix}, \quad \boldsymbol{\mathcal{D}} = \begin{pmatrix} \mathscr{D} & 0 \\ 0 & 0 \end{pmatrix}. \tag{B 3}$$

The parameter c is chosen such that both $\mathcal{A}_1$ and $\mathcal{A}_2$ are self–adjoint and positive definite. Then, it follows that the operator

$$\boldsymbol{\mathcal{A}}u := \begin{pmatrix} \mathcal{A}_1 & 0 \\ 0 & \mathcal{A}_2 \end{pmatrix} \begin{pmatrix} u_1 \\ u_2 \end{pmatrix} = \begin{pmatrix} \mathcal{A}_1 u_1 \\ \mathcal{A}_2 u_2 \end{pmatrix}, \tag{B 4}$$

is also self–adjoint and positive definite. Note that the proof of $\boldsymbol{\mathcal{B}}$ being locally Lipschitz continuous is similar to the one in Akrivis et al. (2011a).

For a general dispersive operator $\boldsymbol{\mathcal{D}}$, the system can be discretised in time by A–stable schemes of at most order 2 - (Akrivis et al. 2011b; Akrivis & Smyrlis 2010). However, this restriction can be removed if the differential operator $\boldsymbol{\mathcal{D}}$ is subdominant with respect to $\boldsymbol{\mathcal{A}}$, in which case multistep schemes of higher orders are stable (up to order 6, see Akrivis et al. (2011a); Akrivis & Smyrlis (2004)). In Fourier space the operator $\mathscr{D}$ has a symbol $\mathcal{N}(k)$ and using the asymptotic property $\mathcal{N}(k) \sim k^2$ as $|k| \to \infty$ (see Appendix A), we establish that $\mathscr{D}$ is subdominant to $\mathcal{A}_1$ whose symbol is proportional to k^4 due to the fourth–order derivative. Consequently, higher order time–stepping schemes are stable and were used in some of our computations.

It is instructive to begin with the localised version of the equations as discussed in Appendix A. Expanding $\mathcal{N}(k)$ for small k up to and including order 3, casts the operators in (B 3) into

$$\mathcal{A}_1 u = \frac{c}{\nu}u + \frac{\Lambda R_e}{60}u_{xx} + \nu u_{xxxx}, \qquad \mathcal{A}_2 u = -\eta\left(u_{xx} - u\right), \tag{B 5}$$

$$\mathscr{D}u = \frac{2\Lambda}{\sqrt{\nu}}\left(u_x - \nu\left(\tfrac{1}{15} + \tfrac{R_e^2}{16800}\right)u_{xxx}\right).$$

Using the usual definition of inner products $(u, v) = \int_0^{2\pi} uv\, dx$, along with periodicity in x, it readily follows that

$$(\mathcal{A}_1 u, v) = (u, \mathcal{A}_1 v), \quad (\mathcal{A}_2 u, v) = (u, \mathcal{A}_2 v), \quad \forall u, v \in H_{per}^4, \tag{B 6}$$

and so $\mathcal{A}_1$ and $\mathcal{A}_2$ are self–adjoint. The operator $\mathcal{A}_2$ is also positive definite since

$$(\mathcal{A}_2 u, u) = \eta\left(\|u\|^2 + \|u_x\|^2\right) \geqslant 0, \quad \forall u \in H_{per}^1. \tag{B 7}$$

For $\mathcal{A}_1$ we find

$$(\mathcal{A}_1 u, u) = \frac{c}{\nu}\|u\|^2 - \frac{\Lambda R_e}{60}\|u_x\|^2 + \nu\|u_{xx}\|^2, \quad \forall\, u \in H^2_{per}, \tag{B 8}$$

which is not always positive definite; the objective is to choose c to make it positive definite. (Note also that we use the result $(\mathcal{D}u, u) = 0$ which holds since $\mathcal{D}$ is an anti-symmetric operator.) Clearly, $\mathcal{A}_1$ is positive definite for any $c > 0$ as long as $\Lambda \leqslant 0$ (in our numerical experiments for this case we take $c = 1$). If $\Lambda > 0$, we proceed by use of Parseval's identity in (B 8) and re–arranging terms (by adding and subtracting $\frac{\Lambda R_e}{60}\|u_x\|^2$ to the right hand side of (B 8)), to find

$$(\mathcal{A}_1 u, u) = 2\pi\nu \sum_k \left(k^4 - \frac{2\Lambda R_e}{60\nu}k^2 + \frac{c}{\nu^2} \right)|\hat{u}_k|^2 + 2\pi\frac{\Lambda R_e}{60}\sum_k k^2|\hat{u}_k|^2. \tag{B 9}$$

Choosing $c = (\frac{\Lambda R_e}{60})^2$ in (B 9) results in

$$(\mathcal{A}_1 u, u) = 2\pi\nu \sum_k \left(k^2 - \frac{\Lambda R_e}{60\nu} \right)^2 |\hat{u}_k|^2 + 2\pi\frac{\Lambda R_e}{60}\sum_k k^2|\hat{u}_k|^2 \geqslant 0, \tag{B 10}$$

proving the desired positive–definite property of $\mathcal{A}_1$.

For the pseudo–differential operator $\mathcal{P}$ that appears in (5.7)–(5.8) we can express the inner product as a Fourier series

$$(\mathcal{P}u, u) = 2\pi\Lambda\nu^{-1/2}\sum_{k=1}^{\infty} k\,\mathrm{Im}\big(F''(0)\big)|\hat{u}_k|^2. \tag{B 11}$$

Numerical solutions of (3.7) show that $\mathrm{Im}\big(F''(0)\big) \leqslant 0$ and so if $\Lambda \leqslant 0$ then $(\mathcal{P}u, u) \geqslant 0$. Setting

$$\mathcal{A}_1 u := \frac{c}{\nu}u + \nu u_{xxxx} + \mathcal{P}u, \tag{B 12}$$

(with $c > 0$, for example $c = 1$ in our computations) and $\mathcal{A}_2$ defined as before in (B 5), ensures that $\boldsymbol{\mathcal{A}}$ is a self–adjoint and positive definite operator. If $\Lambda > 0$ the same definition for $\mathcal{A}_1$ is used but c must be chosen appropriately to ensure the positive–definiteness of $\mathcal{A}_1$. Using the lower bound $\mathrm{Im}\big(F''(0)\big) \geqslant -\left|\min\left\{\mathrm{Im}\big(F''(0)\big)\right\}\right| = -F_{im}$ in (B 11) and inserting the result into

$$(\mathcal{A}_1 u, u) = \frac{c}{\nu}\|u\|^2 + \nu\|u_{xx}\|^2 + (\mathcal{P}u, u), \tag{B 13}$$

we can estimate

$$\frac{c}{\nu}\|u\|^2 + \nu\|u_{xx}\|^2 + (\mathcal{P}u, u) \geqslant 4\pi\nu \sum_{k=1}^{\infty} \left(k^4 - \frac{2\Lambda\nu^{-1/2}}{\nu}F_{im}k^2 + \frac{c}{\nu^2} \right)|\hat{u}_k|^2$$

$$+ 6\pi\sum_{k=1}^{\infty}\Lambda\nu^{-1/2}F_{im}k^2|\hat{u}_k|^2. \tag{B 14}$$

Choosing the constant c to be equal to $c = \left(\Lambda\nu^{-1/2}F_{im}\right)^2$ leads to the desired result

$$(\mathcal{A}_1 u, u) \geqslant \frac{3}{4}\left(\nu\|u_{xx}\|^2 + \frac{\left(\Lambda\nu^{-1/2}F_{im}\right)^2}{\nu}\|u\|^2 \right) \geqslant 0. \tag{B 15}$$

On implementing the scheme, the spatial domain $[0, 2\pi]$ is split into $2M$ equidistant points and the time step is taken to be δt. Letting T be the final time, then $N = T/\delta t$ and

$t_n = n\,\delta t$ for $n = 0, 1, 2, ..., N$ are the time levels at which the solution $\boldsymbol{u}$ will be calculated. The second–order BDF numerical method is given here to define approximations $\boldsymbol{u}^n$ to $\boldsymbol{u}(\cdot, t_n)$ by

$$\frac{3}{2}\boldsymbol{u}^{n+2} + \delta t\,\boldsymbol{\mathcal{L}}\boldsymbol{u}^{n+2} = 2\boldsymbol{u}^{n+1} + 2dt\,\boldsymbol{\mathcal{B}}(\boldsymbol{u}^{n+1}) - \frac{1}{2}\boldsymbol{u}^n - \delta t\,\boldsymbol{\mathcal{B}}(\boldsymbol{u}^n), \qquad (\mathrm{B}\,16)$$

for $n = 0, 1, 2, ..., N - 2$, where $\boldsymbol{\mathcal{L}}$ and $\boldsymbol{\mathcal{B}}$ are defined in (B 2). Note that to start the scheme off we need $\boldsymbol{u}^1$ using the known approximation for $\boldsymbol{u}^0$ from initial conditions. This is achieved by one step of the implicit Euler method. Spatial discretisations are obtained by considering (B 16) in Fourier space. The pseudo–differential operator $\mathcal{P}$ in Fourier space becomes

$$(\widehat{\mathcal{P}u})_k = i\Lambda\nu^{-1}\mathcal{N}(k\sqrt{\nu})\hat{u}_k := id_k\hat{u}_k, \qquad k \in \mathbb{Z}_+. \qquad (\mathrm{B}\,17)$$

Thus (B 16) in Fourier space takes the form

$$\frac{3}{2}\hat{\boldsymbol{u}}_k^{n+2} + \delta t \begin{pmatrix} \frac{c}{\nu} + \nu k^4 + id_k & 0 \\ 0 & \eta k^2 + \eta \end{pmatrix} \hat{\boldsymbol{u}}_k^{n+2} = \left[2I + 2dt \begin{pmatrix} \frac{c}{\nu} & -k^2 \\ 0 & \eta \end{pmatrix} \right] \hat{\boldsymbol{u}}_k^{n+1}$$

$$- \left[\frac{1}{2}I + \delta t \begin{pmatrix} \frac{c}{\nu} & -k^2 \\ 0 & \eta \end{pmatrix} \right] \hat{\boldsymbol{u}}_k^n + 2dt \begin{pmatrix} \hat{A}_k^{n+1} \\ \hat{B}_k^{n+1} \end{pmatrix} - \delta t \begin{pmatrix} \hat{A}_k^n \\ \hat{B}_k^n \end{pmatrix}, \qquad (\mathrm{B}\,18)$$

where $\hat{A}_k$, $\hat{B}_k$ are the Fourier coefficients of $-(H^2/2)_x$ and $-(H\Gamma)_x$ respectively, i.e. $\hat{A}_k = -ik\mathcal{F}(H^2/2)$ and $\hat{B}_k = -ik\mathcal{F}(H\Gamma)$.

In practice, the computations are based on the solution of a $2M \times 2M$ system for the Fourier coefficients $\hat{H}_k$, $\hat{\Gamma}_k$. Note that even when modes evolve to higher frequencies, the nonlinear part of the system is dominated by low frequency modes. This indicates that higher frequencies are 'slaved' by the low frequencies, which is typical in active–dissipative infinite–dimensional dynamical systems (Akrivis et al. 2011a; Akrivis & Smyrlis 2004).

REFERENCES

AKRIVIS, G. & CROUZEIX, M. 2004 Linearly implicit methods for nonlinear parabolic equations. *Math. Comput.*, **73**, 613–635.

AKRIVIS, G., CROUZEIX, M. & MAKRIDAKIS, C. 1998 Implicit–explicit multistep finite element methods for nonlinear parabolic problems. *Math. Comput.*, **67**, 457–477.

AKRIVIS, G., KALOGIROU, A., PAPAGEORGIOU, D. T. & SMYRLIS, Y.-S. 2015 Linearly implicit schemes for multi–dimensional Kuramoto–Sivashinsky type equations arising in falling film flows . *IMA J. Numer. Anal.*. Available from: doi:10.1093/imanum/drv011 .

AKRIVIS, G., PAPAGEORGIOU, D. T. & SMYRLIS, Y.-S. 2011a Linearly implicit methods for a semilinear parabolic system arising in two–phase flows. *IMA J. Numer. Anal.*, **31**, 299–321.

AKRIVIS, G., PAPAGEORGIOU, D. T. & SMYRLIS, Y.-S. 2011b Computational study of the dispersively modified Kuramoto–Sivashinsky equation. *SIAM J. Sci. Comput.*, **34**, A792–A813.

AKRIVIS, G. & SMYRLIS, Y.-S. 2004 Implicit–explicit BDF methods for the Kuramoto–Sivashinsky equation. *Appl. Numer. Math.*, **51**, 151–169.

AKRIVIS, G. & SMYRLIS, Y.-S. 2010 Linearly implicit schemes for a class of dispersive–dissipative systems. *Calcolo*, **48** (2), 145–172.

BARKER, B., JOHNSON, M. A., NOBLE, P., MIGUEL RODRIGUES, L. & ZUMBRUN, K. 2013 Nonlinear modulational stability of periodic traveling–wave solutions of the generalized Kuramoto–Sivashinsky equation. *Physica D*, **258**, 11–46.

BASSOM, A. P., BLYTH, M. G. & PAPAGEORGIOU, D. T. 2010 Nonlinear development of two–

layer Couette–Poiseuille flow in the presence of surfactant. *Phys. Fluids*, **22**, 102102–1 to 102102–15.

BERGÉ, P., POMEAU, Y. & VIDAL, C. 1984 *Order Within Chaos – Towards a Deterministic Approach to Turbulence*. Wiley–Interscience.

BLYTH, M. G. & POZRIKIDIS, C. 2004a Effect of surfactants on the stability of two–layer channel flow. *J. Fluid Mech.*, **505**, 59–86.

BLYTH, M. G. & POZRIKIDIS, C. 2004b Effect of inertia on the Marangoni instability of the two–layer channel flow. Part II: Normal–mode analysis. *J. Eng. Math.*, **50**, 329–341.

CHARRU, F. & HINCH, E. J. 2000 'Phase diagram' of interfacial instabilities in a two–layer Couette flow and mechanism of the long–wave instability. *J. Fluid Mech.*, **414**, 195–223.

CRASTER, R. V. & MATAR, O. K. 2009 Dynamics and stability of thin liquid films. *Rev. Mod. Phys.*, **81**, 1131–1198.

EDWARDS, D. A., BRENNER, H. & WASAN, D. T. 1991 *Interfacial Transport Processes and Rheology*. Butterworth–Heinemann.

FRENKEL, A. L. & HALPERN, D. 2002 Stokes flow instability due to interfacial surfactant. *Phys. Fluids*, **14**, 45–48.

FRENKEL, A. L. & HALPERN, D. 2005 Effect of inertia on the insoluble–surfactant instability of a shear flow. *Phys. Rev. E*, **71**, 016302–1 to 016302–10.

FRENKEL, A. L. & HALPERN, D. 2006 Strongly nonlinear nature of interfacial–surfactant instability of Couette flow. *Intl. J. Pure Appl. Maths*, **29**, 205–224.

FRUMKIN, A. & LEVICH, V. 1947 On surfactants and interfacial motion. *Zhur. Fiz. Khim.* , **21**, 1183–1204. (In Russian.)

FRISCH, U., SHE, Z. H & THUAL, O. 1986 Viscoelastic behaviour of cellular solutions to the Kuramoto–Sivashinsky model. *J. Fluid Mech.*, **168**, 221–240.

HALPERN, D. & FRENKEL, A. L. 2003 Destabilization of a creeping flow by interfacial surfactant: linear theory extended to all wavenumbers. *J. Fluid Mech.*, **485**, 191–220.

HESLA, T. I., PRANCKH, F. R. & PREZIOSI, L. 1986 Squire's theorem for two stratified fluids. *Phys. Fluids*, **29** (9), 2808–2811.

HOOPER, A. P. 1985 Long–wave instability at the interface between two viscous fluids: Thinlayer effects. *Phys. Fluids*, **28**, 1613–1618.

HOOPER, A. P. & BOYD, W. G. C. 1983 Shear–flow instability at the interface between two viscous fluids. *J. Fluid Mech.*, **128**, 507–528.

HOOPER, A. P. & BOYD, W. G. C. 1987 Shear–flow instability due to a wall and a viscosity discontinuity at the interface. *J. Fluid Mech.*, **179**, 201–225.

HOOPER, A. P. & GRIMSHAW, R. 1985 Nonlinear instability at the interface between two viscous fluids. *Phys. Fluids*, **28**, 37–45.

JOSEPH, D. D. & RENARDY, Y. Y. 1992 *Fundamentals of two–fluid dynamics. Part I: Mathematical Theory and applications*. Springer–Verlag, New York.

KALOGIROU, A. 2014 *Nonlinear dynamics of surfactant–laden multilayer shear flows and related systems*. PhD thesis, Imperial College London. Available from: https://spiral.imperial.ac.uk/handle/10044/1/25067.

KALOGIROU, A., PAPAGEORGIOU, D. T. & SMYRLIS, Y.-S. 2012 Surfactant destabilisation and nonlinear phenomena in two–fluid shear flows at small Reynolds numbers. *IMA J. Appl. Math.*, **77**, 351–360.

KALOGIROU, A., KEAVENY, E. E. & PAPAGEORGIOU, D. T. 2015 An in-depth numerical study of the two–dimensional Kuramoto–Sivashinsky equation. *Proc. R. Soc. A*, **471**:20140932.

KAS–DANOUCHE, S. A., PAPAGEORGIOU, D. T. & SIEGEL, M. 2009 Nonlinear dynamics of core–annular flows in the presence of surfactant. *J. Fluid Mech.*, **626**, 415–448.

KEVREKIDIS, I. G., NICOLAENKO, B. & SCOVEL, C. 1990 Back in the saddle again: a computer assisted study of the Kuramoto–Sivashinsky equation. *SIAM J. Appl. Math.*, **50**, 760–790.

LEVICH, V. 1962 *Physicochemical Hydrodynamics*. Prentice Hall.

LI, X. & POZRIKIDIS, C. 1997 The effect of surfactants on drop deformation and on the rheology of dilute emulsions in Stokes flow. *J. Fluid Mech.*, **341**, 165–194.

PAPAGEORGIOU, D. T., MALDARELLI, C. & RUMSCHITZKI, D. S. 1990 Nonlinear interfacial stability of core–annular film flows. *Phys. Fluids A*, **2** (3), 340–352.

PAPAGEORGIOU, D. T., PAPANICOLAOU, G. C. & SMYRLIS, Y.-S. 1992 Modulational stability of

periodic solutions of the Kuramoto–Sivashinsky equation. *Singularities in Fluids, Plasmas and Optics*, NATO ASI Series C, **404**, 255–263. Eds R.E. Caflisch and G.C. Papanicolaou.

POZRIKIDIS, C. 2004 Effect of inertia on the Marangoni instability of two–layer channel flow. Part I: Numerical simulations. *J. Eng. Math.*, **50**, 311–327.

POZRIKIDIS, C. & HILL, A. I. 2011 Surfactant–induced instability of a sheared liquid layer. *IMA J. Appl. Maths*, **76**, 859–875.

RENARDY, Y. Y. 1985 Instability at the interface between two shearing fluids in a channel. *Phys. Fluids*, **28**, 3441–3443.

RENARDY, Y. Y. 1987 The thin–layer effect and interfacial stability in a two–layer Couette flow with similar liquids. *Phys. Fluids*, **30**, 1627–1637.

SAMANTA, A. 2013 Effect of surfactant on two–layer channel flow. *J. Fluid. Mech.*, **735**, 519–552.

SMYRLIS, Y.-S. & PAPAGEORGIOU, D. T. 1998 The effects of generalized dispersion on dissipative dynamical systems. *Appl. Math. Lett.*, **11**, 93–99.

STONE, H. A. & LEAL, L. G. 1990 The effects of surfactants on drop deformation and breakup. *J. Fluid Mech.*, **220**, 161–186.

WEI, H.-H. 2005 Marangoni destabilization on a core–annular film flow due to the presence of surfactant. *Phys. Fluids*, **17**, 027101.

WONG, H., RUMSCHITZKI, D. & MALDARELLI, C. 1996 On the surfactant mass balance at a deforming fluid interface. *Phys. Fluids*, **8**, 3203–3204.

YIH, C.–S. 1967 Instability due to viscosity stratification. *J. Fluid Mech.*, **27**, 337–352.